



Efficient models of polymerization applied to FtsZ ring assembly in *Escherichia coli*

Álvaro Ruiz-Martínez^a, Thomas M. Bartol^b, Terrence J. Sejnowski^{b,c,d,1}, and Daniel M. Tartakovsky^{e,1}

^aDepartment of Mechanical and Aerospace Engineering, University of California, San Diego, La Jolla, CA 92093; ^bComputational Neurobiology Laboratory, Salk Institute for Biological Studies, La Jolla, CA 92037; ^cHoward Hughes Medical Institute, Salk Institute for Biological Studies, La Jolla, CA 92037; ^dThe Division of Biological Studies Sciences, University of California, San Diego, La Jolla, CA 92093; and ^eDepartment of Energy Resources Engineering, Stanford University, Stanford, CA 94305

Contributed by Terrence J. Sejnowski, March 27, 2018 (sent for review November 27, 2017; reviewed by Ajay Gopinathan and Alexander Lukyanov)

High protein concentrations complicate modeling of polymer assembly kinetics by introducing structural complexity and a large variety of protein forms. We present a modeling approach that achieves orders of magnitude speed-up by replacing distributions of lengths and widths with their average counterparts and by introducing a hierarchical classification of species and reactions into sets. We have used this model to study FtsZ ring assembly in *Escherichia coli*. The model's prediction of key features of the ring formation, such as time to reach the steady state, total concentration of FtsZ species in the ring, total concentration of monomers, and average dimensions of filaments and bundles, are all in agreement with the experimentally observed values. Besides validating our model against the in vivo observations, this study fills some knowledge gaps by proposing a specific structure of the ring, describing the influence of the total concentration in short and long kinetics processes, determining some characteristic mechanisms in polymer assembly regulation, and providing insights about the role of ZapA proteins, critical components for both positioning and stability of the ring.

mathematical model | complex kinetics | in vivo concentration | bundling | FtsZ ring assembly

Protein polymerization is central to cell functioning, contributing to cell division, motility, and intracellular transport. In a cell's cytoplasm, interacting monomers form long polymers called filaments, which assemble and disassemble dynamically by elongation and annealing mechanisms. These filaments attach to the cell's membrane and constitute fundamental building elements of the cytoskeleton. In eukaryotic cells, both actin-based microfilaments and tubulin-based microtubules form bundles of different characteristics (1–3). For example, cell migration due to filopodia formation is regulated by the polymerization of long and tight filaments and by their subsequent bundling (1, 4), and F-actin polymerization and bundling are critical processes in the birth, growth, and final form of mushroom-shaped dendritic spines as well as in the guidance and migration of neuronal growth cones (4–7). In prokaryotic cells, such as *Escherichia coli* or *Bacillus subtilis*, FtsZ and MreB proteins (homologues of eukaryotic tubulins and actins) are the most dominant components of their cytoskeletons. Whereas FtsZ is responsible for cell division, MreB controls the cell width. In both eukaryotic and prokaryotic cells, continuous turnover of monomers between the cytosol and the network of polymers regulates the shape and size of filaments and bundles (5, 6, 8–10). Assembly and disassembly of polymers are, therefore, permanent activities even in the steady state.

The importance and ubiquity of polymer assembly provided an impetus for development of its kinetics models, many of which (e.g., refs. 8, 11–15) aim to describe in vivo or in vitro observations of FtsZ assembly. Initial stages of FtsZ polymerization have been adequately captured with the eight-equation model (8, 12). The latter describes only the first seconds of polymerization for different FtsZ strains and buffer conditions, rather than the whole process of FtsZ assembly. The model's failure to

handle later times and in vivo FtsZ concentrations stems from its inability to account for hydrolysis effects and transformations of filaments and bundles. Current models of full FtsZ assembly (e.g., refs. 11, 13, and 15) use hundreds or even thousands of rate equations. Table 1 provides a comparison of these models in terms of their complexity, applicability range, and ability to predict the salient features of FtsZ assembly.

We present a modeling framework that is (many) orders of magnitude faster than the existing alternatives (e.g., those included in Table 1); this speed-up is achieved by replacing distributions of lengths and widths with their average counterparts and by introducing a hierarchical classification of species and reactions into sets. As in previous models, monomers, filaments, and bundles are defined as interacting species; a system of coupled ordinary differential equations (ODEs) describes the temporal evolution of the species concentrations. Unlike those models, our approach involves a hierarchical classification of these species such that, for example, bundles are assembled from filaments that, in turn, are built from monomers. The resulting model comprises ODEs describing the dynamics of the concentrations of species classes and the exchange of elemental quantities (e.g., a monomer in filaments or a filament in bundles) between the classes.

While some kinetic models gain in computational efficiency by replacing filaments of different sizes with filaments of an average length (11, 14, 16), they all treat bundles differing by a single filament as distinct species. Hence, their computational cost increases with total protein concentration, C_{tot} . That is because higher concentrations of C_{tot} result in larger polymers and

Significance

Our modeling framework yields accurate and computationally efficient quantitative predictions of complex kinetics of polymerization processes in biological systems. The resulting model consists of 10 differential equations, regardless of the total concentration of proteins. This is in contrast to previous polymerization models, in which the number of equations increases with the total concentrations, reaching into the thousands. Consequently, our model is orders of magnitude faster than its existing alternatives. It can be used to predict polymerization kinetics at high concentrations characteristic of in vivo processes and, especially, their compartmentalized and spatially distributed representations.

Author contributions: A.R.-M., T.M.B., T.J.S., and D.M.T. designed research; A.R.-M. performed research; and A.R.-M., T.M.B., T.J.S., and D.M.T. wrote the paper.

Reviewers: A.G., University of California, Merced; and A.L., Harvard Medical School.

The authors declare no conflict of interest.

Published under the [PNAS license](#).

¹ To whom correspondence may be addressed. Email: terry@snl.salk.edu or tartakovsky@stanford.edu.

This article contains supporting information online at www.pnas.org/lookup/suppl/doi:10.1073/pnas.1719391115/-DCSupplemental.

Published online April 23, 2018.

Table 1. Comparison of the kinetic in vitro models in terms of their complexity, applicability range, and ability to predict the observed features of FtsZ assembly

Model, reference	(8, 12)	M1 in ref. 11	M2 in ref. 11	M3 in ref. 11	(13)	(14)	AFM
Number of ODEs	8	500	500	1,254	300	17	10
Short time	Yes	Yes	Yes	Yes	Yes	Yes	Yes
Long time	No	Yes	Yes	Yes	Yes	Yes	Yes
Low C_{tot}	Yes	Yes	Yes	Yes	Yes	Yes	Yes
High C_{tot}	No	No	No	No	Yes	Yes	Yes
Filament length	No	Dist	Dist	Ave ⁺	Dist	Ave	Ave
Bundle width	No	No	2 filaments	Dist ⁺	No	Dist	Ave
C_{cr}^1	Yes ⁻	Yes	Yes	Yes	Yes ⁻	Yes	Yes
C_{cr}^2	No	No	No	No	No	Yes	Yes

M1, M2, and M3 designate the single-filament, two-filament bundling, and multifilament bundling models introduced in ref. 11, respectively; AFM denotes our Average Feature Model; C_{tot} is the total concentration of FtsZ monomers in all forms; low and high C_{tot} refers to its values of 2 μ M and 10 μ M, respectively; $C_{cr}^1 = [Z^{na}]_{ss} + [Z]_{ss} \approx 0.7 \mu$ M is the critical concentration at which polymerization begins, and it is computed as the sum of the steady-state concentrations of nonactivated (GDP-bound) and activated (GTP-bound) FtsZ monomers, respectively; $C_{cr}^2 \approx 3.0 \mu$ M is the critical value of concentration C_{tot} at which bundling becomes pronounced. The abbreviations “Ave” and “Dist” denote average and distribution, respectively; the superscripts ⁺ and ⁻ denote the overestimated and underestimated predictions, respectively.

bundles and, consequently, increase the variability of their sizes; the latter enlarges the number of species and ODEs describing their dynamics. At relatively high concentrations, some of the models comprise hundreds or thousands of ODEs (Table 1). In contrast, the number of ODEs in our model (10 or 11, depending on the presence of a membrane) does not change with C_{tot} .

We use in vitro and in vivo FtsZ ring assembly in *E. coli* to demonstrate the veracity and computational efficiency of our model. This complex kinetics process involves a plethora of chemical reactions and species; large concentrations accompanying in vivo assembly of the FtsZ ring put this phenomenon out of reach of most current models. Our approach requires an addition of a single ODE to account for the influence of the membrane and FtsA, ZipA, and ZapA proteins. The resulting 11-ODE model accurately predicts key observed features of the ring formation, such as time to reach the steady state, total concentration of FtsZ species in the ring, total concentration of monomers, and average dimensions of filaments and bundles. It also allows one to generate a hypothesis, for example, about the role of ZapA proteins in positioning and stability of the FtsZ ring.

Average Feature Model of Polymerization

We reduce multiple sizes of polymers to a species called “filament” and “wide bundle” whose average features are tracked in time. The resulting model comprises 10 ODEs. Our model does not provide information about the exact binding sites where species attach or detach. Instead, it estimates variations in concentration of monomers, filaments, and/or bundles. Consequently, we refer to it as an Average Feature Model, or AFM.

The first critical concentration, C_{cr}^1 , is the minimum concentration of FtsZ proteins in the monomeric form at which polymerization begins, and it establishes two regimes of polymerization. The first regime, $C_{tot} \leq C_{cr}^1$, admits only monomers such that $[Z^{na}] + [Z] \approx C_{tot}$, where $[Z^{na}]$ and $[Z]$ denote concentrations of nonactivated (GDP-bound) and activated (GTP-bound) FtsZ monomers, respectively. The second regime, $C_{tot} > C_{cr}^1$, allows for FtsZ polymerization and bundling, with $C_{cr}^1 \approx 0.7 \mu$ M (8).

Short-Time Kinetics. The first protofilaments obtained by combining the corresponding number of monomers are denoted by Z_i with $i = 2, 3$. Longer polymers (i.e., filaments) are denoted by F . The basic structures (monomers, protofilaments, filaments, thin

bundles, and wide bundles) and their graphical representations are summarized in *SI Appendix*, Fig. S1. We describe the early-time kinetics of polymerization with the reduced version (14) of the activation–nucleation–elongation model (8); the latter was used in refs. 16–18 to describe the kinetics of actin polymerization. In so doing, we express the kinetics of all of the processes involved in FtsZ assembly, from its nonactivated monomeric form to long bundles of filaments, in terms of fundamental unimolecular and bimolecular reactions. These are summarized in Table 2 and represented graphically in *SI Appendix*, Fig. S1.

The process of activation is described by reaction I in Table 2, with forward and backward reaction rates k_{ac}^+ and k_{ac}^- , respectively. Activation and deactivation of monomers occurs due to their interactions with GTP and GDP nucleotides, respectively, even though they are not represented explicitly in our model. The process of nucleation is represented by reaction II in Table 2, with forward and backward reaction rates k_{nu}^+ and k_{nu}^- , respectively. Formation of the nucleus of two monomers (nucleation or dimerization) is a critical stage of initialization of the FtsZ assembly (12); it also determines the rate of assembly of the polymer network. The elongation process is modeled by reactions III–V in Table 2, with forward and backward reaction rates k_{el}^+ and k_{el}^- , respectively.

Long-Time Kinetics. The first bundles of k filaments are denoted by B_k with $k = 2, 3$. Bigger structures of laterally attached filaments are referred to as wide bundles and are denoted by

Table 2. Eighteen reactions comprising our FtsZ kinetics model

Reactions	Chemical equations
Reaction I	$Z^{na} \rightleftharpoons Z$
Reaction II	$2Z \rightleftharpoons Z_2$
Reactions III–V	$Z + Z_2 \rightleftharpoons Z_3, Z + Z_3 \rightarrow F, Z + F_{z-} \rightleftharpoons F_{z+}$
Reaction VI	$2F_{f-} \rightleftharpoons F_{f+}$
Reactions VII–XI	$2F \rightleftharpoons B_2, F + B_2 \rightleftharpoons B_3, F + B_3 \rightarrow B_w, F + B_{w;f-} \rightleftharpoons B_{w;f+}, 2B_{w;b-} \rightleftharpoons B_{w;b+}$
Reactions XII and XIII	$F_{z+} \rightarrow F_{z-} + Z^{na}, F_{z+,f+} \rightarrow 2F_{z-,f-} + Z^{na}$
Reactions XIV–XVI	$B_{i;z+,b+} \rightarrow 2B_{i;z-,b-} + Z^{na}, B_{i;z+} \rightarrow B_{i;z-} + Z^{na}, B_{w;z+} \rightarrow B_{w;z-} + Z^{na}$
Reactions XVII and XVIII	$Z + B_{i;z-} \rightarrow B_{i;z+}, Z + B_{w;z-} \rightarrow B_{w;z+}$

The subscripts $z^-/f^-/b^-$ (and $z^+/f^+/b^+$) designate a monomer/filament/bundle lost (or gained) by a species.

B_w . We assume that filaments and bundles have the same length when they connect laterally and that bundles grow laterally into 3D structures. With these simplifications, the process of filament annealing is represented by reaction VI in Table 2, with forward and backward reaction rates k_{an}^+ and k_{an}^- , respectively. The process of filament bundling is modeled similarly to elongation/annealing of filaments; that is, bundles of up to three filaments are explicitly defined by reactions VII–XI in Table 2, with forward and backward reaction rates k_{bu}^+ and k_{bu}^- , respectively. The former rate depends on the number of filaments comprising both reactants; the latter rate varies with the number of filaments comprising the reactant and \bar{L}_{fb}^m , an average filament length (expressed as the number of monomers in a filament)—that is, $k_{bu}^- = k_{bu}^-(\bar{L}_{fb}^m)$.

Hydrolysis of both filaments and bundles contributes to the turnover of monomers between a network of filaments/bundles and the ambient solution.

Dissociation of monomers from filaments after GTP hydrolysis is modeled by irreversible reactions XII and XIII in Table 2, with rates $k_{hy/dis}^1$ and $k_{hy/dis}^2$, respectively. To model dissociation of monomers from bundles after GTP hydrolysis, we supplement the two reactions used in ref. 14 with a third one for wide bundles (reactions XIV–XVI in Table 2). The first of these reactions has rate $k_{hy/dis}^2$, and the remaining two have rate $k_{hy/dis}^3$. Biochemical implications and limitations of our conceptualization of monomer turnover are discussed in ref. 14.

Finally, attachment of monomers to bundles is represented by reactions XVII and XVIII in Table 2, with attachment rate k_{mb} . These reactions account for interactions between activated monomers and the bundles and attachment of the former to the latter.

Concentration of Species Sets. A key component of AFM is a classification of the FtsZ species into different sets (Table 3). Exchange of FtsZ structures between these sets is defined in terms of the elementary reactions collated in Table 2. A set containing all FtsZ species, \mathbb{S}_z , includes monomers (m), filaments (f), and bundles (b) and is endowed with average filament length (\bar{L}_{fb}^m) and bundle width (\bar{f}_{wb}), the number of filaments in a bundle). It comprises a subset of monomers and protofilaments, \mathbb{S}_{mp} , and a subset of filaments and bundles, \mathbb{S}_{fb} , such that $\mathbb{S}_z = \mathbb{S}_{mp} \cup \mathbb{S}_{fb}$. The total concentration (in \mathbb{S}_z) of FtsZ monomers in all forms, C_{tot} , is the sum $C_{tot} = C_{mp}^m + C_{fb}^m$ of the concentration (in \mathbb{S}_{mp}) of monomers in the monomer and protofilament forms and the concentration (in \mathbb{S}_{fb}) of monomers in the filament and bundle forms, with both concentrations defined in Table 3. Transfer of monomers from \mathbb{S}_{mp} to \mathbb{S}_{fb} is due to a reaction set $\mathbb{R}_{mp \rightarrow fb}^m$ (see Table 3). The number of monomers (in both monomer and protofilament forms) involved in reaction R_1 is $m_r^1 = 4$ for the reactants and $m_p^1 = 0$ for the reaction product; the same for reaction R_k ($k = 2, 3, 4$) is $m_r^k = 1$ and $m_p^k = 0$. Likewise, transfer of monomers from \mathbb{S}_{fb} to \mathbb{S}_{mp} is due to a reaction set $\mathbb{R}_{fb \rightarrow mp}^m$. For each reaction R_n ($n = 1, \dots, 6$), $m_r^n = 0$ and $m_p^n = 1$. Then,

$$\frac{dC_{fb}^m}{dt} = \sum_{\substack{k=1 \\ \mathbb{R}_{mp \rightarrow fb}^m}}^4 \kappa_k (m_r^k - m_p^k) - \sum_{\substack{n=1 \\ \mathbb{R}_{fb \rightarrow mp}^m}}^6 \kappa_n (m_p^n - m_r^n), \quad [1]$$

where κ_k ($k = 1, \dots, 10$) are the reaction rates for reactions R_k from the reaction sets $\mathbb{R}_{mp \rightarrow fb}^m$ and $\mathbb{R}_{fb \rightarrow mp}^m$. This formulation conserves mass and energy, although the principle of microscopic reversibility, or detailed balance, is violated (see *SI Appendix, section S1*).

The subset \mathbb{S}_{fb} is, in turn, subdivided into subsets of filaments and thin bundles, \mathbb{S}_{ftb} , and wide bundles, \mathbb{S}_{wb} (see Table 3). The total concentration (in \mathbb{S}_{fb}) of FtsZ filaments in filament and bundle forms, C_{fb}^f , is the sum $C_{fb}^f = C_{ftb}^f + C_{wb}^f$ of the concentration (in \mathbb{S}_{ftb}) of filaments in the filament and thin bundle forms, C_{ftb}^f , and the concentration (in \mathbb{S}_{wb}) of filaments in the wide bundle form, C_{wb}^f . (Both C_{ftb}^f and C_{wb}^f are defined in Table 3.) Transfer of filaments from \mathbb{S}_{ftb} to \mathbb{S}_{wb} is due to a reaction set $\mathbb{R}_{ftb \rightarrow wb}^f$. The number of filaments (in both filament and thin bundle forms) involved in reaction R_1 is $f_r^1 = 4$ for the reactants and $f_p^1 = 0$ for the reaction product; for reaction R_2 , these are $f_r^2 = 1$ and $f_p^2 = 0$. The transfer from \mathbb{S}_{wb} to \mathbb{S}_{ftb} is due to reaction R_3 ; it results in $f_r^3 = 0$ and $f_p^3 = 1$. Then,

$$\frac{dC_{wb}^f}{dt} = \sum_{\substack{k=1 \\ \mathbb{R}_{ftb \rightarrow wb}^f}}^2 \kappa_k (f_r^k - f_p^k) - \sum_{\substack{n=1 \\ \mathbb{R}_{wb \rightarrow ftb}^f}}^1 \kappa_n (f_p^n - f_r^n), \quad [2]$$

where κ_k are the reaction rates for reactions R_k from the reaction sets $\mathbb{R}_{ftb \rightarrow wb}^f$ and $\mathbb{R}_{wb \rightarrow ftb}^f$ (see Table 3).

The definitions of C_{fb}^m and C_{wb}^f relate to the average structural features to the concentrations

$$\bar{L}_{fb}^m = \frac{C_{fb}^m}{[F] + 2[B_2] + 3[B_3] + C_{wb}^f}, \quad \bar{f}_{wb} = \frac{C_{wb}^f}{[B_w]}. \quad [3]$$

A smallest filament consists of four monomers (i.e., has the length $\bar{L}_{fb}^m = 4$). The latter is achieved instantaneously once $[F]$ becomes larger than zero. To consider all species, we define an average total length, \bar{L}_{tot}^m , which includes the first oligomers (Z_2 and Z_3):

$$\bar{L}_{tot}^m = \frac{2[Z_2] + 3[Z_3] + C_{fb}^m}{[Z_2] + [Z_3] + C_{fb}^m / \bar{L}_{fb}^m}. \quad [4]$$

It represents the average length of filaments in all forms (short oligomers, longer filaments, and bundles). Similarly, a smallest wide bundle consists of four filaments (i.e., has the width $\bar{f}_{wb} = 4$). This value is achieved instantaneously once $[B_w]$ becomes larger than zero. To consider all species, we define an average total number of filaments per bundle, \bar{f}_{tot} , which includes the first

Table 3. Species, reaction, and concentration of species sets

Types of sets	Notation
Species sets	$\mathbb{S}_z = \mathbb{S}_{mp} \cup \mathbb{S}_{fb} = \{Z^{na}, Z, Z_2, Z_3, F, B_2, B_3, B_w, m, f, b; \bar{L}_{fb}^m, \bar{f}_{wb}\}$, $\mathbb{S}_{mp} = \{Z^{na}, Z, Z_2, Z_3; m\}$, $\mathbb{S}_{fb} = \mathbb{S}_{ftb} \cup \mathbb{S}_{wb} = \{F, B_2, B_3, B_w, m, f, b; \bar{L}_{fb}^m, \bar{f}_{wb}\}$, $\mathbb{S}_{ftb} = \{F, B_2, B_3; m, f; \bar{L}_{fb}^m\}$, $\mathbb{S}_{wb} = \{B_w; m, f, b; \bar{L}_{fb}^m, \bar{f}_{wb}\}$
Reaction sets	$\mathbb{R}_{mp \rightarrow fb}^m \equiv \{R_1 : IV; R_2 : V_{FW}; R_3 : XVII; R_4 : XVIII\}$, $\mathbb{R}_{fb \rightarrow mp}^m \equiv \{R_1 : V_{BW}; R_2 : XII; R_3 : XIII; R_4 : XIV; R_5 : XV; R_6 : XVI\}$, $\mathbb{R}_{ftb \rightarrow wb}^f \equiv \{R_1 : IX; R_2 : X_{FW}\}$; $\mathbb{R}_{wb \rightarrow ftb}^f \equiv \{R_1 : X_{BW}\}$
Concentrations of species sets	$C_{tot} = C_{mp}^m + C_{fb}^m$, $C_{mp}^m = [Z^{na}] + [Z] + 2[Z_2] + 3[Z_3]$, $C_{fb}^m = \bar{L}_{fb}^m ([F] + 2[B_2] + 3[B_3] + \bar{f}_{wb}[B_w])$, $C_{fb}^f = C_{ftb}^f + C_{wb}^f$, $C_{ftb}^f = [F] + 2[B_2] + 3[B_3]$, $C_{wb}^f = \bar{f}_{wb}[B_w]$

FW and BW designate forward and backward reactions, respectively.

Table 4. Timing of FtsZ ring formation for a characteristic range of in vivo FtsZ concentrations, $C_{\text{tot},C;0} = 6 - 18 \mu\text{M}$

$C_{\text{tot},C;0}, \mu\text{M}$	t_{att}, s	$t_{\bar{L}}, \text{s}$	t_{mon}, s	$t_{\bar{f}}, \text{s}$
6.0	19	49	220	244
12.0	10	53	217	240
18.0	8	40	210	233

oligomers (Z_2 and Z_3), longer filaments (F), and the first thin bundles (B_2 and B_3):

$$\bar{f}_{\text{tot}} = \frac{2[Z_2] + 3[Z_3] + C_{\text{fb}}^m}{2[Z_2] + 3[Z_3] + \bar{L}_{\text{fb}}^m([F] + [B_2] + [B_3] + [B_w])}. \quad [5]$$

Average characteristics \bar{L}_{fb}^m , \bar{L}_{tot}^m , \bar{f}_{wb} , and \bar{f}_{tot} play a crucial role in reducing the number of species and, therefore, the number of equations used to describe the protein assembly process. *SI Appendix, section S1* contains ODEs corresponding to the reactions involved in the short- and long-term kinetics processes described above.

Model's Calibration, Validation, and Computational Cost. The system of 10 ODEs is parametrized and calibrated on the steady-state, low-concentration ($C_{\text{tot}} = 0.7 - 3.0 \mu\text{M}$) data from ref. 8 (see *SI Appendix, section S2*). The resulting model is validated by comparing its fit-free predictions with the transient, low-concentration data and the steady-state high-concentration ($C_{\text{tot}} = 3.0 - 10.0 \mu\text{M}$) data, both from ref. 8 (*SI Appendix, section S3*). This comparison demonstrates AFM's ability to accurately predict time evolution of nonactivated and activated monomers, the first critical concentration C_{cr}^1 at which polymerization begins, an average size of filaments and bundles, and the second critical concentration C_{cr}^2 at which bundles appear.

This predictive power of AFM is achieved at a fraction of the cost of its nearest competitor (14), which, in turn, is orders of magnitude faster than the models consisting of hundreds of ODEs (see Table 1). The computational efficiency of AFM, vis-à-vis ref. 14 and other models of this kind, is magnified when it is used to simulate in vivo polymerization phenomena, which are characterized by high total concentrations. For $C_{\text{tot}} = 200 \mu\text{M}$, AFM is about 2 orders of magnitude faster than ref. 14 (see *SI Appendix, section S4* for details).

FtsZ-Ring Assembly in *E. coli*. We use AFM to describe the Z-ring formation in the middle of an *E. coli* cell, within a torus adjacent to the cell membrane (CM) of volume V_{CM} . A typical cell has a volume $V_{\text{CELL}} = 1.374 \mu\text{m}^3$ and contains 5000 - 15000 FtsZ molecules, which translates into a range of FtsZ concentrations in the cytosol, $C_{\text{tot},C;0} = 6 - 18 \mu\text{M}$ (19-21); at the midcell, close to the membrane, the concentration is one to two orders of magnitude higher than that. Only a few polymerization models can handle such concentrations, and even the most computationally efficient among them (14) (Table 1) would require hundreds of ODEs to handle all bundle sizes. AFM accomplishes the same with 11 ODEs, adding only one equation for the total concentration of FtsZ species (in all forms) attached to the membrane, $C_{\text{tot},\text{CM}}^{\text{a}}$.

CM contributes to significant physical, chemical, and structural differences between in vitro and in vivo polymerization. The augmented AFM accounts for some of these differences by incorporating the FtsZ species' attachment to and detachment from a CM. The parameters relevant to this process as well as other parameters describing cell geometry and bundling/dissociation kinetics come from the literature, so that predictions reported below are made without any fitting param-

eters. (A detailed formulation of the augmented AFM is provided in *SI Appendix, section S5*.)

Timing of FtsZ Ring Formation. We define four stages of the ring formation in terms of their characteristic times: time it takes the FtsZ protofilaments in the cytoplasm to attach to the mid-CM and occupy all binding sites, t_{att} ; time to reach a constant average length of all filaments and bundles in the ring, $t_{\bar{L}}$; time to reach a constant concentration of monomers at the midcell region ($C_{\text{m},\text{CM}}^{\text{d}}$), t_{mon} ; and time to reach a constant average number of filaments per bundle in the ring, $t_{\bar{f}}$.

Let P denote an FtsZ ring property and P^∞ its value at $t \rightarrow \infty$; P stands for $C_{\text{tot},\text{CM}}^{\text{a}}$ at time t_{att} , \bar{L}_{tot}^m at time $t_{\bar{L}}$, $C_{\text{m},\text{CM}}^{\text{d}}$ at time t_{mon} , and \bar{f}_{tot} at time $t_{\bar{f}}$. We compute these times by inverting the condition $|P(t) - P^\infty|/P^\infty < 0.01$. The results, reported in Table 4, reveal that changes in the total concentration $C_{\text{tot},C;0}$ appreciably affect t_{att} (early-time kinetics), while having an almost negligible impact on the other three characteristic times (long-time kinetics). These results identify the timing for three distinct stages of the ring formation (time $t = 0$ corresponds to the moment at which the Ter region is already located at the center of the cell).

Short-time kinetics. Attachment of FtsZ protofilaments to the binding sites at the midcell takes 8 to 19 s. Although there are no data about the first seconds of in vivo polymerization to verify this prediction, the values that our model estimates are quite similar to the turnover half-times of FtsA (12 to 16.3 s) (22) and ZipA mutants [7.81 to 9.01 s, or 0.111 to 0.128 s^{-1}] (23), which is the range of FtsZ turnover rate values, since according to ref. 24 both FtsZ and ZipA may undergo similar dynamic exchanges]. It seems reasonable to think that the emergence of the first FtsZ oligomers at the membrane will depend strongly on the time that FtsA and ZipA, both responsible for the attachment of FtsZ to the membrane, remain themselves attached to the membrane.

Intermediate kinetics. Elongation of the species up to their average length takes 40 to 50 s. This is in line with the observations (25, 26) that ring assembly takes ~ 1 min. This suggests correspondence between the complete longitudinal elongation of the species and the ring formation.

Long-time kinetics. Continuous exchange of monomers between the ring and the cytosol accompanies the formation of large FtsZ structures, at 3.5 to 4 min. This is consistent with the observed time interval, ~ 4 min, between the ring's central positioning and the onset of septation (27). These findings imply that dissociation of monomers after GTP hydrolysis plays a fundamental role in rearrangement of filaments and bundles, while formation of wide bundles contributes to regulation of the dissociation in live cells, just as it does in in vitro studies (14). Finally, the timing predictions obtained with our model and the in vivo version of ref. 14 are compared in *SI Appendix, section S4*.

FtsZ Ring Features. Our model predicts FtsZ concentrations in the ring to be around 40 times larger than cytosolic concentrations (Table 5). Variations in the total concentration $C_{\text{tot},C;0}$ do not materially affect the average length of the species at steady state, $\bar{L}_{\text{tot}}^m = 24$ to 25 monomers. That value corresponds to the experimentally observed characteristic length of 120 to 125 nm (since the monomer's diameter is 5 nm) (8) and falls within

Table 5. FtsZ ring features for a characteristic range of in vivo FtsZ concentrations, $C_{\text{tot},C;0} = 6 - 18 \mu\text{M}$, at steady state ($t \rightarrow \infty$)

$C_{\text{tot},C;0}, \mu\text{M}$	$C_{\text{tot},\text{CM}}^{\text{a}}, \mu\text{M}$	\bar{L}_{tot}^m	$C_{\text{m},\text{CM}}^{\text{d}}, \mu\text{M}$	\bar{f}_{tot}
6.0	237	24.43	1.13	9.4
12.0	474	24.47	1.20	16.4
18.0	711	24.49	1.25	22.7

Table 6. Large FtsZ structures for a range of in vivo FtsZ concentrations, $C_{\text{tot},C;0} = 6 - 18 \mu\text{M}$

$C_{\text{tot},C;0}, \mu\text{M}$	$\mathcal{R}_{\text{wb}}^{\%}$	\bar{f}_{clu}	\bar{f}_{CLS}	$\mathcal{N}_{\text{clu}}^{\text{CLS}}$	\mathcal{N}_{CLS}	\mathcal{N}_{clu}
6.0	85.1	6.1	19.6	3.2	2.8	9.0
12.0	91.6	7.6	35.0	4.6	3.4	15.6
18.0	94.0	9.5	48.5	5.1	3.7	18.9

The structures are characterized by the percentage of FtsZ proteins in the wide-bundles form, $\mathcal{R}_{\text{wb}}^{\%}$; the average number of filaments per bundle in a cluster, \bar{f}_{clu} ; average width of CLSs, \bar{f}_{CLS} ; number of clusters per CLS, $\mathcal{N}_{\text{clu}}^{\text{CLS}}$; number of CLSs, \mathcal{N}_{CLS} ; and number of clusters, \mathcal{N}_{clu} .

the range, 100 – 200 nm, found in other in vitro experiments (28–30).

The predicted steady-state concentration of attached monomers, $C_{\text{tot},\text{CM}}^{\text{a},\infty} = 0.9$ to $1.25 \mu\text{M}$, is insensitive to the total concentration $C_{\text{tot},C;0}$ (Table 5) and falls within the range of values of the first critical concentration in wild-type cells, $C_{\text{cr},\text{wt}}^1$ (12). We postulate this feature to be representative of polymer assembly regulation, both in in vitro and in in vivo.

The total cytosolic concentration $C_{\text{tot},C;0}$ does affect the average number of filaments per bundle at steady state, $\bar{f}_{\text{tot}}^{\infty}$ (Table 5). To investigate the prevalence of this form of FtsZ proteins at steady state, we consider the percentage of FtsZ proteins in the form of wide bundles, $\mathcal{R}_{\text{wb}}^{\%} \equiv 100\% \times C_{\text{wb},\text{CM}}^{f,\text{a}} / ([F] + 2[B_2] + 3[B_w] + C_{\text{wb},\text{CM}}^{f,\text{a}})$. Table 6 reveals that, at steady state, $\mathcal{R}_{\text{wb}}^{\%} = 85\% - 94\%$, depending on $C_{\text{tot},C;0}$; that is, wide bundles are the dominant species.

Once $C_{\text{tot},\text{CM}}^{\text{a}} = C_{\text{tot},\text{CM}}^{\text{a,max}}$ —that is, all FtsZ protofilaments are attached to the mid-CM—bundles form cross-linked structures (CLSs) along the ring. We refer to these structures as “clusters,” which in our model are formed at time $t = t_{\text{att}}$ and consist of bundles with an average number of filaments $\bar{f}_{\text{clu}} = \bar{f}_{\text{tot}}(t_{\text{att}})$. The predicted values $\bar{f}_{\text{clu}} = 6.1 - 9.5$ (Table 6) imply the average width of FtsZ–ZapA sheets of 12.2 – 19. This is consistent with the experimentally observed maximal number of FtsZ–ZapA filaments perfectly aligned at the mid-CM, $\bar{f}_{\text{clu},\text{ZapA}} < \bar{f}_{\text{wb},\text{ZapA}}^{\text{max}} = 20$ (see *SI Appendix, section S7* for details). The predicted minimal value, $\bar{f}_{\text{clu},\text{ZapA}} = 12.2$, indicates that the two-layered sheets have to occupy at least half of the axial width of the ring. When that occurs, bundle interactions in the tangential direction, which induce bundles to push and lift each other, dominate their axial interactions.

For $t > t_{\text{att}}$, \bar{f}_{clu} remains constant as clusters interact only along the ring-forming CLSs. Since wide bundles contain most of the FtsZ at steady state, we define an average CLS width as $\bar{f}_{\text{CLS}} = \bar{f}_{\text{wb}}(t \rightarrow \infty)$. A number of clusters per CLS is $\mathcal{N}_{\text{clu}}^{\text{CLS}} \equiv \bar{f}_{\text{CLS}} / \bar{f}_{\text{clu}}$, and a number of CLSs is $\mathcal{N}_{\text{CLS}} \equiv [B_w] V_{\text{CM}} N_A / 10^{21}$, where N_A is Avogadro’s number. A number of clusters in the entire ring is $\mathcal{N}_{\text{clu}} = \mathcal{N}_{\text{clu}}^{\text{CLS}} \mathcal{N}_{\text{CLS}}$. Our model predicts $\mathcal{N}_{\text{clu}} = 9.0 - 18.9$ (Table 6), which conforms to the observed range of 10 – 20 clusters (31).

To sum up, our model predicts FtsZ rings that are mostly composed of 3 to 4 large structures, which are partially attached to the membrane and comprise 3 to 5 cross-linked clusters each. These clusters contain 6 to 10 filaments made up of 24 monomers each. The entire network also includes ZapA tetramers, which reinforce the lateral bonds of the clusters and the cross-links between clusters, as observed in vitro (32) and in vivo (33). *SI Appendix, section S4* includes a comparison between the ring feature predictions of our model and the in vivo version of ref. 14.

ZapA Deficiency. A recent experimental study (33) investigated in vivo polymerization in the absence of ZapA proteins. Our model

predicts the resulting FtsZ concentrations to be only 10 times larger than their in vitro counterparts (Table 7). The average length (L_{tot}^m) and concentration ($C_{\text{m},\text{CM}}^{\text{d}}$) of detached monomers are insensitive to the total cytosolic concentration $C_{\text{tot},C;0}$. The predicted monomer concentrations $C_{\text{m},\text{CM}}^{\text{d}}$ fall within the experimentally observed range of critical concentrations, $C_{\text{tot},\text{CM}}^{\text{a},\infty} = 0.9 - 1.25 \mu\text{M}$.

The model also predicts the predominant presence of non-cross-linked and dispersed thin clusters along the entire cell, as observed (33). In the absence of ZapA, $t_{\text{att}} = 20 - 30$ s is twice as long as that in the case with ZapA, while $t_{\text{L}} = 40 - 50$ s remains about the same. The times for bundling and dissociation of monomers after GTP hydrolysis, $t_{\text{mon}} \sim t_{\text{f}} = 100 - 120$ s, are half of their counterparts in the presence of ZapA. Since FtsZ structures are more dispersed and interactions happen less frequently, the equilibrium is reached faster.

Conclusions

We developed a computationally efficient model of protein polymerization, which relies on concentrations and average features of different species. Orders of magnitude speed-up is achieved by replacing distributions of lengths and widths with their average counterparts and by introducing a hierarchical classification of species and reactions into sets. The resulting model consists of 10 or 11 ODEs, regardless of the total concentration of proteins. This is in contrast to previous polymerization models, in which the number of ODEs increases with the total concentrations, reaching into the thousands. Consequently, our model can be used to predict polymerization kinetics at high concentrations characteristic of in vivo processes and, especially, their compartmentalized representations.

We have used this model to study in vitro and in vivo FtsZ ring assembly in *E. coli*, a complex kinetics process with a large number of chemical reactions and species involved. The model’s computational performance is not affected by the large concentrations of proteins located at the midcell, near the membrane. The model’s predictions of key features of the ring formation, such as time to reach the steady state, total concentration of FtsZ species in the ring, total concentration of monomers, and average dimensions of filaments and bundles, are all in agreement with the experimentally observed values. Besides validating our model against the in vivo observations, this study fills some knowledge gaps by proposing a specific structure of the ring, describing the influence of the total concentration in short and long kinetics processes, determining some characteristic mechanisms in polymer assembly regulation, and providing insights about the role of ZapA proteins, a critical component for both positioning and stability of the ring.

The orders of magnitude computational speed-up provided by our model comes at a cost. An explicit representation of bundle size distribution (14) would improve a description of the ring’s structure (e.g., heterogeneity of the bundle network). It would avoid overestimation of robustness at the sides of the ring where proteins like MinC promote debundling and depolymerization (29). The influence of bundling on the dissociation of monomers upon the GTP-hydrolysis process is also related to the size of the

Table 7. FtsZ species features for a characteristic range of in vivo FtsZ concentrations, $C_{\text{tot},C;0} = 6 - 18 \mu\text{M}$, in the absence of ZapA at steady state

$C_{\text{tot},C;0}, \mu\text{M}$	$C_{\text{tot},\text{CM}}^{\text{a,max}}, \mu\text{M}$	L_{tot}^m	$C_{\text{m},\text{CM}}^{\text{d}}, \mu\text{M}$	\bar{f}_{tot}
6.0	48	35.43	0.92	1.92
12.0	104	35.84	0.95	3.49
18.0	160	35.86	1.00	4.76

bundles, which is captured by the model (14). Nevertheless, our results demonstrate that the models based on average characteristics yield predictions at least as accurate as those computed with their distribution-based model counterparts.

1. Dixon RD, et al. (2008) Palladin is an actin cross-linking protein that uses immunoglobulin-like domains to bind filamentous actin. *J Biol Chem* 283:6222–6231.
2. Erb ML, et al. (2014) A bacteriophage tubulin harnesses dynamic instability to center DNA in infected cells. *eLife* 3:6222–6231.
3. Walczak CE, Shaw SL (2010) A MAP for bundling microtubules. *Cell* 142:433–443.
4. Mattila PK, Lappalainen P (2008) Filopodia: Molecular architecture and cellular functions. *Nat Rev Mol Cell Biol* 9:446–454.
5. Koskinen M, Hotulainen P (2014) Measuring F-actin properties in dendritic spines. *Front Neuroanat* 8:1–14.
6. Medeiros NA, Burnette DT, Forscher P (2006) Myosin II functions in actin-bundle turnover in neuronal growth cones. *Nat Cell Biol* 8:216–226.
7. Penzes P, Rafalovich I (2012) Regulation of the actin cytoskeleton in dendritic spines. *Adv Exp Med Biol* 970:81–95.
8. Chen Y, Erickson HP (2005b) Rapid in vitro assembly dynamics and subunit turnover of FtsZ demonstrated by fluorescence resonance energy transfer. *J Biol Chem* 280:22549–22554.
9. Chen Y, Erickson HP (2009) FtsZ filament dynamics at steady state: Subunit exchange with and without nucleotide hydrolysis. *Biochemistry* 48:6664–6673.
10. Rottner K, Stradal TEB (2011) Actin dynamics and turnover in cell motility. *Curr Opin Cell Biol* 23:569–578.
11. Lan G, Dajkovic A, Wirtz D, Sun SX (2008) Polymerization and bundling kinetics of FtsZ filaments. *Biophys J* 95:4045–4056.
12. Chen Y, Bjornson K, Redick SD, Erickson HP (2005a) A rapid fluorescence assay for FtsZ assembly indicates cooperative assembly with a dimer nucleus. *Biophys J* 88:505–514.
13. Surovtsev IV, Morgan JJ, Lindhal PA (2008) Kinetic modeling of the assembly, dynamic steady state and contraction of the FtsZ ring in prokaryotic cytokinesis. *PLoS Comput Biol* 4: e1000102.
14. Ruiz-Martinez A, Bartol TM, Sejnowski TJ, Tartakovsky DM (2016) Efficient multiscale models of polymer assembly. *Biophys J* 110:185–196.
15. Dow CE, Rodger A, Roper DI, van den Berg HA (2013) A model of membrane contraction predicting initiation and completion of bacterial cell division. *Integr Biol* 5:778–795.
16. Falzone TT, Lenz M, Kovar DR, Gardel ML (2012) Assembly kinetics determine the architecture of α -actin in crosslinked F-actin networks. *Nat Commun* 3:266–272.
17. Frieden C, Goddette DW (1983) Polymerization of actin and actin-like systems: Evaluation of the time course of polymerization in relation to the mechanism. *Biochemistry* 22:5836–5843.
18. Sept D, Xu J, Pollard TD, McCammon JA (1999) Annealing accounts for the length of actin filaments formed by spontaneous polymerization. *Biophys J* 77:2911–1919.
19. Hale CA, de Boer AJ (1997) Direct binding of FtsZ to ZipA, an essential component of the septal ring structure that mediates cell division in *E. coli*. *Cell* 88:175–185.
20. Rueda S, Vicente M, Mingorance J (2003) Concentration and assembly of the division ring proteins FtsZ, FtsA, and ZipA during the *Escherichia coli* cell cycle. *J Bacteriol* 185:3344–3351.
21. Erickson HP, Anderson DE, Osawa M (2010) FtsZ in bacterial cytokinesis: Cytoskeleton and force generator all in one. *Microbiol Mol Biol Rev* 74:504–528.
22. Geissler B, Shiomi D, Margolin W (2007) The ftsA* gain-of-function allele of *Escherichia coli* and its effects on the stability and dynamics of the Z ring. *Microbiology* 153:814–825.
23. Anderson DE, Gueiros-Filho FJ, Erickson HP (2004) Assembly dynamics of FtsZ rings in *Bacillus subtilis* and *Escherichia coli* and effects of FtsZ-regulating proteins. *J Bacteriol* 186:5775–5781.
24. Stricker J, Maddox P, Salmon ED, Erickson HP (2002) Rapid assembly dynamics of the *Escherichia coli* FtsZ-ring demonstrated by fluorescence recovery after photobleaching. *Proc Natl Acad Sci USA* 99:3171–3175.
25. Addinall CSG, Cao C, Lutkenhaus J (1997) Temperature shift experiments with an ftsZ84(Ts) strain reveal rapid dynamics of FtsZ localization and indicate that the Z ring is required throughout septation and cannot reoccupy division sites once constriction has initiated. *J Bacteriol* 179:4277–4284.
26. Sun Q, Margolin W (1998) FtsZ dynamics during the division cycle of live *Escherichia coli* cells. *J Bacteriol* 180:2050–2056.
27. Tsukanov R, et al. (2011) Timing of Z-ring localization in *Escherichia coli*. *Phys Biol* 8:066003.
28. Romberg L, Simon M, Erickson HP (2001) Polymerization of FtsZ, a bacterial homolog of tubulin: Is assembly cooperative? *J Biol Chem* 276:11743–11753.
29. Dajkovic A, Lan G, Sun SX, Wirtz D, Lutkenhaus J (2008) MinC spatially controls bacterial cytokinesis by antagonizing the scaffolding function of FtsZ. *Curr Biol* 18:235–244.
30. Popp D, Iwasa M, Narita A, Erickson HP, Maéda Y (2009) FtsZ condensates: An in vitro electron microscopy study. *Biopolymers* 91:340–350.
31. Coltharp C, Buss J, Plumer TM, Xiao J (2016) Defining the rate-limiting processes of bacterial cytokinesis. *Proc Natl Acad Sci USA* 113:1044–1053.
32. Dajkovic A, Pichoff S, Lutkenhaus J, Wirtz D (2010) Cross-linking FtsZ polymers into coherent Z rings. *Mol Microbiol* 78:651–668.
33. Buss J, et al. (2013) In vivo organization of the FtsZ-ring by ZapA and ZapB revealed by quantitative super-resolution microscopy. *Mol Microbiol* 89:1099–1120.

ACKNOWLEDGMENTS. This work was supported in part by the Howard Hughes Medical Institute, National Institutes of Health Grants MH079076 and P41-GM103712, the Salk Innovation Award, the Defense Advanced Research Projects Agency EQUiPS program, and National Science Foundation Grant DMS-1620103.

S1. ODEs for *in vitro* Systems

Basic structures (monomers, protofilaments, filaments, thin bundles and wide bundles) and their graphical representations are summarized in Figure S1. The reactions involved in the short- and long-time kinetics of polymerization and bundling are described in the eponymous sections. The concentrations, $[\cdot]$, of non-activated (Z^{na}) and activated (Z) monomers, dimers (Z_2) and trimers (Z_3) satisfy a system of ODEs,

$$\frac{d[Z^{\text{na}}]}{dt} = -k_{\text{ac}}^+[Z^{\text{na}}] + k_{\text{ac}}^-[Z] + k_{\text{hy/dis}}^1[F] + k_{\text{hy/dis}}^2([F] + [B_2] + [B_3]) + k_{\text{hy/dis}}^3\Sigma_B, \quad [\text{S1}]$$

$$\frac{d[Z]}{dt} = k_{\text{ac}}^+[Z^{\text{na}}] - k_{\text{ac}}^-[Z] - 2k_{\text{nu}}^+[Z]^2 + 2k_{\text{nu}}^-[Z_2] - k_{\text{el}}^+[Z]([Z_2] + [Z_3] + [F]) + k_{\text{el}}^-([Z_3] + [F]) - k_{\text{mb}}[Z]\Sigma_B, \quad [\text{S2}]$$

$$\frac{d[Z_2]}{dt} = k_{\text{nu}}^+[Z]^2 - k_{\text{nu}}^-[Z_2] - k_{\text{el}}^+[Z][Z_2] + k_{\text{el}}^-[Z_3], \quad [\text{S3}]$$

$$\frac{d[Z_3]}{dt} = k_{\text{el}}^+[Z]([Z_2] - [Z_3]) - k_{\text{el}}^-[Z_3]. \quad [\text{S4}]$$

where $\Sigma_B \equiv [B_2] + [B_3] + [B_w]$.

Filaments (F) and thin bundles (B_2 and B_3) are assumed to be present in the same concentrations regardless of their length. Consequently, we set $[F] \equiv [F_{z-}] = [F_{z+}] = [F_{f-}] = [F_{f+}] = [F_{z-,f-}] = [F_{z+,f+}]$, $[B_i] \equiv [B_{i;z-}] = [B_{i;z+}] = [B_{i;b-}] = [B_{i;b+}] = [B_{i;z-,b-}] = [B_{i;z+,b+}]$ with $i = 2, 3$. Likewise, wide bundles (B_w) are assumed to be present in the same concentrations regardless of their length and number of filaments, so that $[B_w] \equiv [B_{w;z-}] = [B_{w;z+}] = [B_{w;b-}] = [B_{w;b+}] = [B_{w;z-,b-}] = [B_{w;z+,b+}]$. Thus, we only define ODEs for $[F]$, $[B_2]$, $[B_3]$ and $[B_w]$,

$$\frac{d[F]}{dt} = k_{\text{el}}^+[Z][Z_3] - k_{\text{an}}^+[F]^2 + k_{\text{an}}^-[F] - k_{\text{bu}}^+[F](2[F] + \Sigma_B) + k_{\text{bu}}^-([B_2] + \Sigma_B) + k_{\text{hy/dis}}^2[F], \quad [\text{S5}]$$

$$\frac{d[B_2]}{dt} = k_{\text{bu}}^-([B_3] - [B_2]) + k_{\text{bu}}^+[F]([F] - [B_2]) + k_{\text{hy/dis}}^2[B_2], \quad [\text{S6}]$$

$$\frac{d[B_3]}{dt} = -k_{\text{bu}}^-[B_3] + k_{\text{bu}}^+[F]([B_2] - [B_3]) + k_{\text{hy/dis}}^2[B_3], \quad [\text{S7}]$$

$$\frac{d[B_w]}{dt} = k_{\text{bu}}^+[F][B_3] - k_{\text{bu}}^+[B_w]^2 + k_{\text{bu}}^-[B_w]. \quad [\text{S8}]$$

Finally, the concentration of monomers in long filaments and bundles (C_{fb}^m) and the concentration of filaments in wide bundles (C_{wb}^f) satisfy

$$\frac{dC_{\text{fb}}^m}{dt} = 4k_{\text{el}}^+[Z][Z_3] + k_{\text{el}}^+[Z][F] - k_{\text{el}}^-[F] - k_{\text{hy/dis}}^1[F] - k_{\text{hy/dis}}^2([F] + [B_2] + [B_3]) - k_{\text{hy/dis}}^3\Sigma_B + k_{\text{mb}}[Z]\Sigma_B, \quad [\text{S9}]$$

$$\frac{dC_{\text{wb}}^f}{dt} = 4k_{\text{bu}}^+[F][B_3] - k_{\text{bu}}^-[B_w] + k_{\text{bu}}^+[F][B_w]. \quad [\text{S10}]$$

Eqs. S1–S10 are subject to initial conditions $[Z^{\text{na}}]_0 = C_{\text{tot}}$, $[Z]_0 = 0$, $[Z_i]_0 = 0$, $[F]_0 = 0$, $[B_i]_0 = 0$, $[B_w]_0 = 0$, $C_{\text{fb},0}^m = 0$ and $C_{\text{wb},0}^f = 0$, with $i = 2, 3$. These equations form a system of ten ODEs, which is solved with a combination of fourth- and fifth-order Runge-Kutta methods for non-stiff ODEs, implemented in ODE45 Matlab function.

Conservation of mass. Recall that the total concentration of FtsZ monomers in all forms, C_{tot} , is the sum $C_{\text{tot}} = C_{\text{mp}}^m + C_{\text{fb}}^m$ of the concentration of monomers in the monomer and protofilament forms, $C_{\text{mp}}^m = [Z^{\text{na}}] + [Z] + 2[Z_2] + 3[Z_3]$, and the concentration of monomers in the filament and bundle forms, $C_{\text{fb}}^m = \bar{L}_{\text{fb}}^m([F] + 2[B_2] + 3[B_3] + \bar{f}_{\text{wb}}[B_w])$. It follows from this definition of C_{mp}^m and Eqs. S1–S4 that

$$\frac{dC_{\text{mp}}^m}{dt} = -k_{\text{el}}^+[Z](4[Z_3] + [F]) + k_{\text{el}}^-[F] + k_{\text{hy/dis}}^1[F] + k_{\text{hy/dis}}^2([F] + [B_2] + [B_3]) + k_{\text{hy/dis}}^3\Sigma_B - k_{\text{mb}}[Z]\Sigma_B. \quad [\text{S11}]$$

Combining Eqs. S9 and S11 with the definitions of C_{tot} and C_{fb}^m yields

$$\frac{dC_{\text{tot}}}{dt} = 0. \quad [\text{S12}]$$

This proves conservation of the total concentration of FtsZ monomers in all forms, C_{tot} .

Conservation of energy. In common with (1), our model does not satisfy the detailed (net cycle) balance. That is because the turnover of monomers between the polymer structure and the solution is a nonequilibrium steady-state process (NESS), which violates the detailed balance. While the reactions we used to model the assembly/disassembly of FtsZ monomers constitute a NESS and satisfy the net cycle balance, the irreversible reactions describing the dissociation of monomers from filaments and bundles imply consumption of energy and conformational changes that destabilize the polymers (2).

Regardless of the nonequilibrium steady state, artificial irreversible reactions $Z + Z_3 \rightarrow F$ and $F + B_3 \rightarrow B_w$ provide a coarsened representation of a transition between a model for short-time kinetics, which describes how fast monomers assemble, and a model for long-time kinetics, which represent slow processes such as annealing, bundling or disassembly of monomers following GTP hydrolysis. For a more detailed discussion, we refer the interested reader to (1) and the references therein.

S2. Model Parametrization

We use the *in vitro* study (3) of FtsZ-F268C polymerization to determine values of the reaction rates in ODEs S1–S10. The study covers a wide range of FtsZ concentrations, and its findings are in agreement with other investigations.

POLYMER STRUCTURE	GRAPHICAL REPRESENTATION
<i>Non-activated monomer, Z^{na}</i>	
<i>Activated monomer, Z</i>	
<i>Protofilaments, Z_2, Z_3</i>	
<i>Long filaments, F</i>	
<i>Thin bundles, B_2, B_3</i>	
<i>Wide bundles, B_w</i>	
REACTION	GRAPHICAL REPRESENTATION
<i>Activation</i>	
<i>Nucleation</i>	
<i>Elongation</i>	
<i>Filament annealing</i>	
<i>Filament bundling</i>	
<i>Dissociation of non-activated monomers from filaments following GTP hydrolysis</i>	
<i>Dissociation of non-activated monomers from bundles following GTP hydrolysis</i>	
<i>Attachment of monomers to bundles</i>	

Fig. S1. Graphical representation of basic polymer structures and reactions.

All but four parameter values are taken from the literature (Table S1). The remaining four are estimated with a model calibration procedure described in the end of this section. The calibration is carried out on the steady-state, low-concentration ($C_{\text{tot}} = 0.7\text{-}3.0 \mu\text{M}$) data from (3).

Table S1. Reaction rate constants and bond energies. The energy units are expressed in terms of the Boltzmann constant k_B and room temperature T .

Parameter	Units	Value	Reference
k_{ac}^+	s^{-1}	0.38	(3)
k_{ac}^-	s^{-1}	0.01	(3)
k_{nu}^+	$\mu\text{M}^{-1}\text{s}^{-1}$	0.79	(3)
k_{nu}^-	s^{-1}	199.8	(3)
k_{el}^+	$\mu\text{M}^{-1}\text{s}^{-1}$	6.6	(3)
k_{an}^+	$\mu\text{M}^{-1}\text{s}^{-1}$	6.6	(3)
k_{bu}^{0+}	$\mu\text{M}^{-1}\text{s}^{-1}$	4.0955	Calibrated
k_{bu}^{0-}	s^{-1}	199.9704	Calibrated
k_{mb}	$\mu\text{M}^{-1}\text{s}^{-1}$	2.1957	Calibrated
$k_{\text{hss/dis}}^1$	s^{-1}	0.6998	Calibrated
$k_{\text{hss/dis}}^2$	s^{-1}	0.143	(3)
$k_{\text{hss/dis}}^3$	s^{-1}	0.112	(4)
ΔU_t	$k_B T$	4.05	(3, 5)
ΔU_m	$k_B T$	8.10	(5)
U_b	$k_B T$	0.175	(5, 6)
ΔU_b	$k_B T$	0.0405	(5, 6)

Following (1, 3, 7) and reducing the number of elongation steps from 5 to 2, we assume the forward (k_{el}^+) and backward (k_{el}^-) reaction rates to be independent of a filament length (i.e., to be the same for all i). This is in contrast to the variable bundling rates $k_{bu}^{\pm} = k_{bu}^{\pm}(\bar{f}_{R_1}, \bar{f}_{R_2}; R_1, R_2, P)$ of a generic bundling reaction,



between two linear chain molecules R_i ($i = 1, 2$) with average number of filaments \bar{f}_{R_i} , which diffuse and bind laterally to produce a species P . The bundling process, when it occurs, is mainly diffusion-limited (1). We show in Section S6 that, for any two reactants R_i from the set $\{F, B_2, B_3, B_w\}$, the forward bundling rate, $k_{bu}^+(\bar{f}_{R_1}, \bar{f}_{R_2}; R_1, R_2, P)$, is given by

$$k_{bu}^+ = \frac{1}{2} k_{bu}^{0+} F_F(\bar{f}_F) \sum_{i=1}^2 \frac{1}{\sqrt[3]{\bar{f}_{R_i} F_{R_i}(\bar{f}_{R_i})}}, \quad [\text{S14a}]$$

where

$$\bar{f}_{R_i} = \begin{cases} 1 & \text{if } R_i = F \\ 2 & \text{if } R_i = B_2 \\ 3 & \text{if } R_i = B_3 \\ \bar{f}_{wb} & \text{if } R_i = B_w \end{cases}, \quad i = 1, 2; \quad [\text{S14b}]$$

and

$$F_{R_i} = \sum_{k=0}^7 a_k x_{R_i}^k, \quad x_{R_i} = \frac{1}{2} \ln[3/(2\bar{f}_{R_i})], \quad [\text{S14c}]$$

with values of the constants a_k provided in Section S6. The lateral association rate of two filaments, k_{bu}^{0+} , corresponds to a reaction involving $R_1 = F$ and $R_2 = F$, such that Eq. S14 yields $k_{bu}^+ = k_{bu}^{0+}$. A value of k_{bu}^{0+} is uncertain but must fall within the accepted range of protein-protein association rates, $2.0 - 7.5 \mu\text{M}^{-1}\text{s}^{-1}$ (3, 4, 8). It is determined with our model calibration procedure. Rate expression S14 is valid for polymers whose size satisfies the requirement $\bar{f}_{R_i} \in [1.5 \times 10^{-4}, 1.5 \times 10^4]$. This is not overly restrictive, since $\bar{f}_{R_i} < 1.5 \times 10^{-4}$ is equivalent to the absence of filaments and bundles (in which case $k_{bu}^+ \equiv 0$), and $\bar{f}_{R_i} > 1.5 \times 10^4$ is not observed in the experiments (3).

Our model achieves an orders-of-magnitude computational speed-up by postulating that both elongation and bundling processes can be reduced to just a few steps (up to bundles of three filaments, in the case of bundling). We demonstrate the accuracy of this approximation in Section S3.

The depolymerization reaction rates, k_{el}^- , k_{an}^- and k_{bu}^- , are determined from the respective internal energies of filaments and bundles. Specifically, the backward reaction rates for elongation and annealing are given by (5)

$$k_{el}^- = k_{nu}^- e^{-\Delta U_t} \quad \text{and} \quad k_{an}^- = k_{nu}^- e^{-\Delta U_m}, \quad [\text{S15}]$$

where ΔU_t and ΔU_m are the increments in the energy of a monomer connected at the end and middle of a filament, respectively. The value of ΔU_t is calculated from the first expression in Eq. S15, with the values for k_{nu}^- and k_{el}^- taken from (3). Conservation of energy suggests (5) that $\Delta U_m = 2\Delta U_t$.

The variable lateral dissociation rates k_{bu}^- in Eq. S13 are computed as (Section S6)

$$k_{bu}^- = k_{bu}^{0-} \begin{cases} 1 & \bar{L}_{fb}^m \leq 1 \\ e^{-(\bar{L}_{fb}^m - 1)U_b} & \bar{L}_{fb}^m > 1 \end{cases} \quad \text{for } P = B_2 \quad [\text{S16}]$$

and

$$k_{bu}^- = k_{bu}^{0-} e^{-\Delta U_b} \begin{cases} 1 & \bar{L}_{fb}^m \leq 1 \\ e^{-(\bar{L}_{fb}^m - 1)(U_b + \Delta U_b)} & \bar{L}_{fb}^m > 1 \end{cases} \quad \text{for } P = B_3. \quad [\text{S17}]$$

The backward reaction with $P \equiv B_w$, $R_1 = F$ and $R_2 = B_w$ in Eq. S13 does not take place ($k_{bu}^- = 0$) until $\bar{f}_{wb} > 1.5 \times 10^{-4}$. After that, in the range of bundle sizes $\bar{f}_{wb} \in (1.5 \times 10^{-4}, 1.5 \times 10^4)$,

$$k_{bu}^- = k_{bu}^{0-} e^{-26(U_b + \Delta U_b) - \Delta U_b}. \quad [\text{S18}]$$

Finally, reaction Eq. S13 with $P = B_w$, $R_1 = B_w$ and $R_2 = B_w$ is shown to be practically irreversible within the given parameter range, i.e., its rate is $k_{bu}^- = 0$. The bond energy per lateral bond, U_b , is set to $U_b = 0.175 k_B T$, which represents both the average of the values reported in (6) for the same strain as in (3) but a different buffer and the value used in (5) for a strain different from (3) but for the same buffer. Experimental evidence (5, 6) suggests that the bond energy per longitudinal bond is around 100 times larger than the bond energy per lateral bond. Assuming that increments of longitudinal and lateral energies keep the same proportion, we obtain $\Delta U_t/\Delta U_b \sim 100$, which gives $\Delta U_b = 0.0405 k_B T$. The reference dissociation rate k_{bu}^{0-} is one of the four parameters used for model calibration. In the absence of experimental

evidence, we have explored a wide range of its values (0.0 – 500 s⁻¹) during the model calibration.

The choice of the remaining parameters is identical to that in (1). Dissociation of monomers following GTP hydrolysis is essentially absent in the beginning of polymerization (3, 9), and becomes more pronounced as the amount of polymers increases and they interact more frequently with GDP. This dependence of the hydrolysis/dissociation rates on the polymer concentrations is accounted for as

$$k_{\text{hy/dis}}^i = k_{\text{hss/dis}}^i \frac{C_{\text{tot}} - [Z^{\text{na}}] - [Z]}{C_{\text{tot}} - C_{\text{cr}}^1}, \quad i = 1, 2, 3, \quad [\text{S19}]$$

where $C_{\text{cr}}^1 < C_{\text{tot}}$ in the second regime of polymerization. At the beginning of the assembly process, most FtsZ proteins are in the form of nonactivated (Z^{na}) and activated (Z) monomers, such that $[Z^{\text{na}}] + [Z] \approx C_{\text{tot}}$ and $k_{\text{hy/dis}}^i \rightarrow 0$. At steady-state, when the polymer network is formed and GDP deactivates monomers more often, these rates reach their maximum values, $k_{\text{hy/dis}}^i \approx k_{\text{hss/dis}}^i$ for $i = 1, 2, 3$.

The reaction rates controlling dissociation after GTP hydrolysis depend on the location of a deactivated monomer in the filament or bundle. In Table S1, $k_{\text{hss/dis}}^i$ ($i = 1, 2, 3$) denote values of the hydrolysis rates for filaments and bundles at steady-state. Only the rate for detachment of monomers from filament ends, $k_{\text{hss/dis}}^1$, was calibrated. The rate for detachment of monomers from the middle of filaments and thin bundles, $k_{\text{hss/dis}}^2$, is set to the average value reported in (3) for turnover of monomers at steady state (half-time of 7 s, i.e., 0.143 s⁻¹), because we assume that it is the depolymerization reaction that happens more often. This assumption is based on two facts: the predominant species observed in the experiment are filaments and thin bundles, and there are more monomers in the middle of filaments and bundles than in their ends. The value of $k_{\text{hss/dis}}^3$ is determined in (4) by observing the detachment of non-activated monomers from thick bundles. These three rates satisfy the following order relations. It takes less energy to break a longitudinal bond at the filament end than two bonds at its middle, therefore, $k_{\text{hss/dis}}^1 > k_{\text{hss/dis}}^2$ (10). We use this condition for calibration of $k_{\text{hss/dis}}^1$. The values of $k_{\text{hss/dis}}^2$ for shortening of filaments and thin bundles are equal, because both reactions describe the loss of a monomer in the middle of a filament. The value of $k_{\text{hss/dis}}^3$ is the smallest of the three rates, since the monomers in a bundle can be doubly connected both longitudinally and laterally. In the absence of wide bundles, i.e., for $\bar{f}_{\text{wb}} \leq 1.5 \times 10^{-4}$, $k_{\text{hss/dis}}^3 = 0$.

The rate at which activated monomers in the solution attach themselves to bundles is quantified by the reaction rate constant k_{mb} . The latter serves as the final calibration parameter; its computed value (Table S1) falls within the range of values of the protein-protein interaction rates of 2–7.5 $\mu\text{M}^{-1}\text{s}^{-1}$. The condition $k_{\text{mb}} < k_{\text{el}}^+ = 6.6 \mu\text{M}^{-1}\text{s}^{-1}$ is also imposed during calibration, because pure longitudinal attachments of monomers to filament ends are more favorable than combinations of both longitudinal and lateral attachments in a monomer-bundle interaction. In the absence of wide bundles, i.e., for $\bar{f}_{\text{wb}} \leq 1.5 \times 10^{-4}$, k_{mb} is assumed to be zero.

Model calibration procedure. The steady-state experiments reported in (3) reveal that

- the amount of FtsZ in monomer form equals the first critical concentration, $C_{\text{cr}}^1 = 0.7 \mu\text{M}$, regardless of the value of C_{tot} in the range between 0.7 μM and 3.0 μM ;

- the average length of filaments and bundles at $C_{\text{tot}} = 2.0 \mu\text{M}$ is $\bar{L}_{\text{tot}} = 120.0 \text{ nm}$. Since the diameter of FtsZ monomers is 4.0 – 5.0 nm (3, 11, 12), this corresponds to $\bar{L}_{\text{tot}}^m = 24 - 30$, i.e., the average length of filaments comprising 24 – 30 monomers;

- the value of \bar{L}_{tot}^m remains practically unchanged for $C_{\text{tot}} = 3.0 \mu\text{M}$; and

- the majority of filaments are single-stranded at all levels of C_{tot} in the range between 0.7 μM and 3.0 μM . This suggests an average number of filaments per bundle to be no larger than $\bar{f}_{\text{tot}} = 1.5$.

These observations serve to constrain the model calibration. We employ the Matlab optimization routine `fmincon`, which enables one to find minima of constrained nonlinear multivariable functions. Our calibration procedure is similar to that in (3) and consists of the following steps.

1. Define the coupled functionals to be minimized at steady state:

(a) Eqs. S1–S10 with the time derivatives set to 0;

(b) $([Z^{\text{na}}] + [Z]) - C_{\text{cr}}^1$;

(c) $C_{\text{fb}}^m - \bar{L}_{\text{fb}}^m([F] + 2[B_2] + 3[B_3] + C_{\text{wb}}^f)$;

(d) $\bar{f}_{\text{tot}} - \frac{\sum_{i=2}^3 i[Z_i] + \bar{L}_{\text{fb}}^m([F] + \sum_{i=2}^3 i[B_i] + \bar{f}_{\text{wb}}[B_w])}{\sum_{i=2}^3 i[Z_i] + \bar{L}_{\text{fb}}^m([F] + \sum_{i=2}^3 [B_i] + [B_w])}$.

2. Define a set of C_{tot} -dependent constraints (for $C_{\text{tot}} = 0.7, 0.8, 1.0, 1.5, 2.0, 2.5$, and 3.0 μM):

(a) lower and upper bounds for the parameters to be calibrated (Table S2);

(b) lower and upper bounds for the monomer concentration, average length and average number of filaments per bundle (Table S3);

(c) order relations for the average length, $\bar{L}_{\text{fb}}^m(C_{\text{tot}})$, and number of filaments per bundle, $\bar{f}_{\text{tot}}(C_{\text{tot}})$: the higher the total concentration C_{tot} (in μM), the longer and wider the filaments and bundles are, i.e., $\bar{L}_{\text{fb}}^m(0.7) < \bar{L}_{\text{fb}}^m(0.8) < \bar{L}_{\text{fb}}^m(1.0) < \bar{L}_{\text{fb}}^m(1.5) < \bar{L}_{\text{fb}}^m(2.0) < \bar{L}_{\text{fb}}^m(2.5) < \bar{L}_{\text{fb}}^m(3.0)$ and $\bar{f}_{\text{tot}}(0.7) < \bar{f}_{\text{tot}}(0.8) < \bar{f}_{\text{tot}}(1.0) < \bar{f}_{\text{tot}}(1.5) < \bar{f}_{\text{tot}}(2.0) < \bar{f}_{\text{tot}}(2.5) < \bar{f}_{\text{tot}}(3.0)$.

3. Make initial guesses for the optimization variables (Table S2) and functionals (see Table S4).

4. Estimate the parameters by run `fmincon` with the Sequential Quadratic Programming algorithm, `sqp`, and tolerance 10^{-8} . Use the estimates as new initial guesses and repeat 20 times to get an accurate calibration.

This calibration procedure yields the values of k_{bu}^{0+} , k_{bu}^{0-} , k_{mb} and $k_{\text{hss/dis}}^1$ reported in Table S1.

Table S2. Lower and upper bounds, and initial guesses, for the kinetic parameters used in the model calibration procedure.

	k_{bu}^{0+} ($\mu\text{M}^{-1}\text{s}^{-1}$)	k_{bu}^{0-} (s^{-1})	k_{mb} ($\mu\text{M}^{-1}\text{s}^{-1}$)	$k_{hss/dis}^1$ (s^{-1})
Lower bound	2.0	0.0	2.0	0.143
Upper bound	7.5	500.0	6.6	∞
Initial guess	4.0	200.0	2.0	0.7

Table S3. Lower and upper bounds for the concentrations (in μM , with $i = 2, 3$ and $j = 2, 3$), average length and average number of filaments per bundle, informed by the data in (3).

	$[Z^{na}]$	$[Z]$	$[Z_i]$	$[F]$	$[B_j]$	$[B_w]$	C_{fb}^m	C_{wb}^f	\bar{L}_{fb}^m	\bar{f}_{tot}
Lower bound ($C_{tot} = 0.7 \mu\text{M}$)	0.0	0.0	0.0	0.0	0.0	0.0	0.0	0.0	1	1
Upper bound ($C_{tot} = 0.7 \mu\text{M}$)	∞	∞	∞	∞	∞	∞	0.0	∞	1	1
Lower bound ($C_{tot} = 0.8 \mu\text{M}$)	0.0	0.0	0.0	0.0	0.0	0.0	0.1	0.0	1	1
Upper bound ($C_{tot} = 0.8 \mu\text{M}$)	∞	∞	∞	∞	∞	∞	0.1	∞	27	1.5
Lower bound ($C_{tot} = 1.0 \mu\text{M}$)	0.0	0.0	0.0	0.0	0.0	0.0	0.3	0.0	1	1
Upper bound ($C_{tot} = 1.0 \mu\text{M}$)	∞	∞	∞	∞	∞	∞	0.3	∞	27	1.5
Lower bound ($C_{tot} = 1.5 \mu\text{M}$)	0.0	0.0	0.0	0.0	0.0	0.0	0.8	0.0	1	1
Upper bound ($C_{tot} = 1.5 \mu\text{M}$)	∞	∞	∞	∞	∞	∞	0.8	∞	27	1.5
Lower bound ($C_{tot} = 2.0 \mu\text{M}$)	0.0	0.0	0.0	0.0	0.0	0.0	1.3	0.0	24	1
Upper bound ($C_{tot} = 2.0 \mu\text{M}$)	∞	∞	∞	∞	∞	∞	1.3	∞	30	1.5
Lower bound ($C_{tot} = 2.5 \mu\text{M}$)	0.0	0.0	0.0	0.0	0.0	0.0	1.8	0.0	24	1
Upper bound ($C_{tot} = 2.5 \mu\text{M}$)	∞	∞	∞	∞	∞	∞	1.8	∞	30	1.5
Lower bound ($C_{tot} = 3.0 \mu\text{M}$)	0.0	0.0	0.0	0.0	0.0	0.0	2.3	0.0	24	1
Upper bound ($C_{tot} = 3.0 \mu\text{M}$)	∞	∞	∞	∞	∞	∞	2.3	∞	30	1.5

Table S4. Initial guesses of the concentrations (in μM , with $i = 2, 3$), average length and average number of filaments per bundle.

C_{tot} (μM)	$[Z^{na}]$	$[Z]$	$[Z_i]$	$[F]$	$[B_i]$	$[B_w]$	C_{fb}^m	C_{wb}^f	\bar{L}_{fb}^m	\bar{f}_{tot}
0.7	0.0	0.0	0.0	0.01	0.01	0.01	0.0	0.0	1	1
0.8	0.0	0.0	0.0	0.01	0.01	0.01	0.1	0.0	5	1
1.0	0.0	0.0	0.0	0.01	0.01	0.01	0.3	0.0	10	1
1.5	0.0	0.0	0.0	0.01	0.01	0.01	0.8	0.0	18	1.02
2.0	0.0	0.0	0.0	0.01	0.01	0.01	1.3	0.0	25	1.04
2.5	0.0	0.0	0.0	0.01	0.01	0.01	1.8	0.0	27	1.08
3.0	0.0	0.0	0.0	0.01	0.01	0.01	2.3	0.0	28	1.11

S3. Model Validation

With the parameter values fixed in the previous section, we use our model (hereafter referred to as Average-Features Model or AFM) to obtain fit-free predictions of the FtsZ polymerization dynamics at low concentration ($C_{\text{tot}} = 0.7 - 3.0 \mu\text{M}$) and its steady-state limit at high concentrations ($C_{\text{tot}} = 3.0 - 10.0 \mu\text{M}$). Comparison with the corresponding data from the Fluorescence Resonance Energy Transfer experiment (3) serves to validate the model.

Transient, low-concentration phenomena.

Short-time kinetics. Annealing, bundling and GTP-hydrolysis/dissociation reactions are thought to be absent during the first seconds of polymerization. The experiment (3) yielded information about the temporal evolution of FtsZ-F268C that assembles into filaments or bundles. Fluorescence is defined in terms of the concentrations of non-activated (Z^{na}) and activated (Z) monomers as $\mathcal{F} = \alpha_1([Z^{\text{na}}] + [Z]) + \alpha_2(C_{\text{tot}} - [Z^{\text{na}}] - [Z])$, where the parameters α_1 and α_2 represent the fluorescence of monomers and proteins in polymer form, respectively. Figure S2 exhibits the temporal evolution of \mathcal{F} for $C_{\text{tot}} = 1.22, 1.98$ and $3.12 \mu\text{M}$ observed in (3) and predicted with AFM. The agreement between the two indicates the model's validity at early times. The plateau of the intensity curves corresponds to the situation in which all FtsZ-F268C proteins are assembled, except for monomers with concentration similar to the first critical concentration, $C_{\text{cr}}^1 = 0.7 \mu\text{M}$. Although C_{cr}^1 is the same regardless of C_{tot} , the fluorescence intensities for each plateau are different. That is because the fluorescence \mathcal{F} is proportional to the amount of polymerized FtsZ-F268C and the latter increases with C_{tot} . The agreement between the data and AFM confirms that the reduced version of elongation process (up to trimers) is sufficient to make accurate predictions.

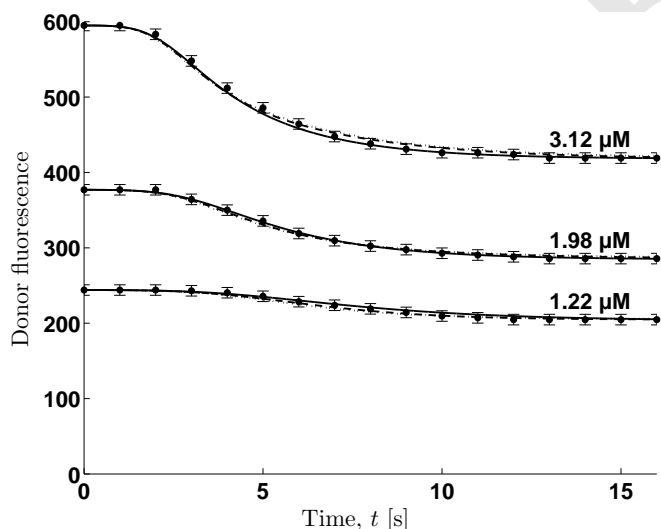


Fig. S2. Kinetics of the initial FtsZ-F268C assembly observed in (3), for three values of total concentration C_{tot} . The data points and compared with predictions of the models in (3) (solid lines) and (1) (dashed lines), as well as with those of AFM (dotted lines). The agreement between the three models is to be expected since annealing, bundling and GTP-hydrolysis/dissociation, all which are not accounted for in the model (3), do not become pronounced until the later stages of polymerization.

Long-time kinetics. The predicted steady-state statistics of FtsZ assembly, i.e., \bar{L}_{tot}^m , \bar{f}_{tot} and $C_{\text{cr}}^1 = [Z^{\text{na}}]_{\text{ss}} + [Z]_{\text{ss}}$, are compared with their observed counterparts in Table S5. Since the steady-state data were used for parameter identification, it is to be expected that the steady-state model predictions are in agreement with observations (3): the average length for $C_{\text{tot}} = 2.0 - 3.0 \mu\text{M}$ is between 24 and 30 monomers; the majority of the filaments are single-stranded for low concentrations, i.e., $\bar{f}_{\text{tot}} < 1.5$ for $C_{\text{tot}} < 3.0 \mu\text{M}$; and $[Z^{\text{na}}]_{\text{ss}} + [Z]_{\text{ss}} = 0.7 \mu\text{M}$, which coincides with the value reported in (3) for C_{tot} in the range between $0.7 \mu\text{M}$ and $3.0 \mu\text{M}$. While such an agreement is not surprising, it is worthwhile pointing out that the model in (3), which was designed to reproduce these experiments, underestimates the first critical concentration, yielding $[Z^{\text{na}}]_{\text{ss}} + [Z]_{\text{ss}} \approx 0.5 \mu\text{M}$. This underestimation is due to both the dissociation of monomers from filaments following GTP hydrolysis and the effects of bundling on the turnover rate. These two processes are explicitly accounted for in our model, but are absent in the CE model. The agreement between the data and AFM confirms that the reduced version of bundling process (up to bundles of three filaments) is sufficient to make accurate predictions.

Steady-state, high-concentration phenomena.

Average size of filaments and bundles. Under physiologically relevant conditions, $C_{\text{tot}} = 5.0 - 10.0 \mu\text{M}$, AFM captures the observed tendency of filaments to keep fixed length, $\bar{L}_{\text{tot}}^m \approx 32 - 33$ subunits at steady-state, regardless of the value of C_{tot} . Tables S5 and S6 show that, for $C_{\text{tot}} = 2.0 - 10.0 \mu\text{M}$, the predicted average length is $\bar{L}_{\text{tot}}^m = 25 - 33$ subunits (125 - 165 nm), which is within the well established range of 100 - 200 nm (6, 11, 13-16).

Almost all filaments remain single-stranded when $C_{\text{tot}} < 2.0 \mu\text{M}$ (Table S5). For larger concentrations, up to $C_{\text{tot}} = 10.0 \mu\text{M}$, and for various buffers and FtsZ strains, filaments dominate and the majority of bundles consist of two filaments. All the computed values of \bar{f}_{tot} in Table S6 are below 2, which is in agreement not only with (3) but also with other experiments (6, 14, 16, 17).

Concentration of monomers at steady state. In the physiologically relevant range of $C_{\text{tot}} = 5.0 - 10.0 \mu\text{M}$, AFM predicts the steady-state concentration of monomers to be $[Z^{\text{na}}]_{\text{ss}} + [Z]_{\text{ss}} \approx 0.7 \mu\text{M}$ (Table S6). This matches the observed monomer concentration (3) and equals the first critical concentration, C_{cr}^1 . The model presented in (3) underestimates this observation, predicting a value of $[Z^{\text{na}}]_{\text{ss}} + [Z]_{\text{ss}} \approx 0.5 \mu\text{M}$.

Second critical concentration. An appreciable decrease in the fluorescence intensity at $C_{\text{tot}} = 3.0 \mu\text{M}$ (or, more generally, at $C_{\text{tot}} = 2.0 - 4.0 \mu\text{M}$, depending on the concentration of Mg^{2+} contained in the buffer) was observed, but not explained, in (3). A subsequent kinetics model (5) utilized the experimental data from (13) and (3) to describe this phenomenon by identifying a critical concentration, C_{cr}^2 , at which the presence of bundles becomes pronounced. The model in (5) does not specify the value of C_{cr}^2 and, crucially, predicts formation of bundles comprised two or three filaments at low concentrations ($C_{\text{tot}} = 2.0 \mu\text{M}$), which is not supported by the observations. Our model correctly predicts the ratio of an average number of monomers per filaments to an average number of filaments per bundle for a range of C_{tot} . This ratio reaches its maximum at

Table S5. Steady-state average length (\bar{L}_{tot}^m), number of filaments per bundle (\bar{f}_{tot}) and monomer concentration ($[Z^{\text{na}}]_{\text{ss}}+[Z]_{\text{ss}}$), predicted by (1), (3) and AFM, and observed in the low-concentration experiment (3).

C_{tot} (μM)	\bar{L}_{tot}^m			\bar{f}_{tot}			$[Z^{\text{na}}]_{\text{ss}}+[Z]_{\text{ss}}$ (μM)			
	(1)	AFM	Observed	(1)	AFM	Observed	(3)	(1)	AFM	Observed
1.0	7	7	< 27	1.0	1.0	< 1.5	0.526	0.701	0.710	0.7
2.0	25	24	24 – 30	1.1	1.0	< 1.5	0.534	0.699	0.712	0.7
3.0	30	29	24 – 30	1.3	1.1	< 1.5	0.536	0.695	0.701	0.7

Table S6. Steady-state average length (\bar{L}_{tot}^m), number of filaments per bundle (\bar{f}_{tot}) and monomer concentration ($[Z^{\text{na}}]_{\text{ss}}+[Z]_{\text{ss}}$), predicted by (1), (3) and AFM, and observed in the high-concentration experiment (3).

C_{tot} (μM)	\bar{L}_{tot}^m			\bar{f}_{tot}			$[Z^{\text{na}}]_{\text{ss}}+[Z]_{\text{ss}}$ (μM)			
	(1)	AFM	Observed	(1)	AFM	Observed	(3)	(1)	AFM	Observed
4.0	31.42	30.42	30	1.39	1.18	< 2	0.537	0.693	0.694	0.7
5.0	32.14	31.13	30	1.50	1.26	< 2	0.538	0.691	0.690	0.7
6.0	32.55	31.51	30	1.60	1.37	< 2	0.538	0.690	0.689	0.7
7.0	32.81	31.76	30	1.69	1.49	< 2	0.539	0.690	0.688	0.7
8.0	32.99	31.93	30	1.77	1.62	< 2	0.539	0.689	0.687	0.7
9.0	33.12	32.05	30	1.84	1.75	< 2	0.539	0.689	0.687	0.7
10.0	33.21	32.15	30	1.91	1.89	< 2	0.539	0.690	0.687	0.7

$C_{\text{tot}} = 3.5 \mu\text{M}$, the critical concentration C_{cr}^2 after which the longitudinal growth (elongation and/or annealing) ceases to dominate the lateral growth (bundling) and bundles become an important factor in the overall kinetics (Fig. S3). Our predicted value of $C_{\text{cr}}^2 = 3.5 \mu\text{M}$ falls within the experimentally observed range of $2 - 4 \mu\text{M}$.

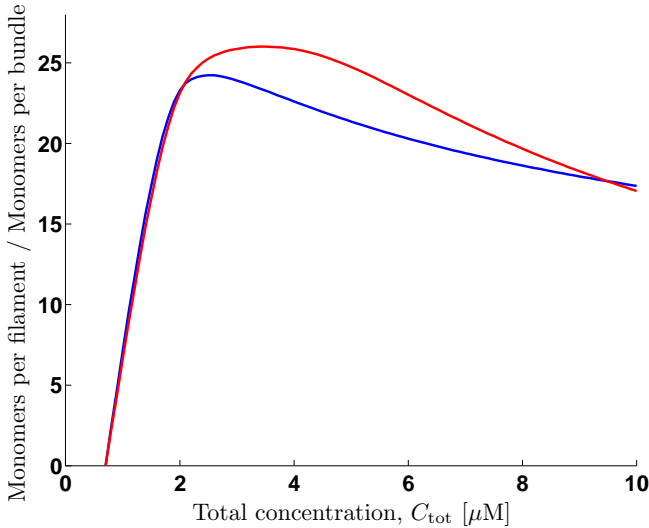


Fig. S3. Monomers per filament-to-Filaments per bundle ratio at steady state predicted by (1) (blue line) and AFM (red line), for a range of concentration C_{tot} .

S4. Comparison of Computational Costs

The maximum number of filaments per bundle increases with the total concentration of FtsZ monomers in all forms, C_{tot} . The resulting growth in the number of bundle sizes requires more ODEs comprising the model (1), which raises the latter's computational cost (Fig. S4). The computational time required to reach steady-state with the model (1) increases linearly with

the total concentration in both *in vitro* ($C_{\text{tot}} = 0.7 - 20 \mu\text{M}$, left column of Fig. S4) and *in vivo* ($C_{\text{tot}} = 0.7 - 200 \mu\text{M}$, right column of Fig. S4) regimes. Thus, the computational cost of the simulations of the first 40 s of *in vitro* polymerization increases six-fold as C_{tot} increases from $0.7 \mu\text{M}$ to $20 \mu\text{M}$. This degradation in the computational efficiency of the model (1) is due to the concomitant increase in both the number of species and in the number of ODEs needed to describe their dynamics (Fig. S4). This is in contrast to AFM, which comprises 10 ODEs regardless of the value of total concentration C_{tot} . Consequently, its computational cost remains the same over the full range of C_{tot} ; it is more than half of the lowest computational cost of the model (1) with $C_{\text{tot}} = 0.7 \mu\text{M}$.

The computational efficiency of our model is magnified when it is used to simulate *in vivo* polymerization phenomena, which are characterized by high total concentrations. For $C_{\text{tot}} = 200 \mu\text{M}$, AFM is about two orders-of-magnitude faster than its competitor (1) (right column of Fig. S4).

Comparison of *in vivo* predictions. From all previous works presented in Table 1, we see that (1) is able to make accurate predictions for the range of concentrations $C_{\text{tot}} = 3 - 10 \mu\text{M}$. By averaging the concentration and size of bundles, we have seen that AFM makes similar predictions at a lower computational cost. In Section S5, we present variations associated to *in vivo* assembly to our *in vitro* AFM version such as the influence of the membrane or the presence of FtsA, ZipA and ZapA proteins. Introducing those modifications in the *in vitro* model from (1), we can compare both models and see that our current work improves the applicability range, the ability to predict ring features and the computational cost in a complex *in vivo* scenario.

All variations presented in S5 are introduced in (1) except the ones related to the bundling rates that are inherent to AFM. We keep the constant values for forward bundling rates from (1) and modify the backward bundling rate to be able to introduce the influence of ZapA protein. Our study in (1) did not distinguish between the different backward bundling

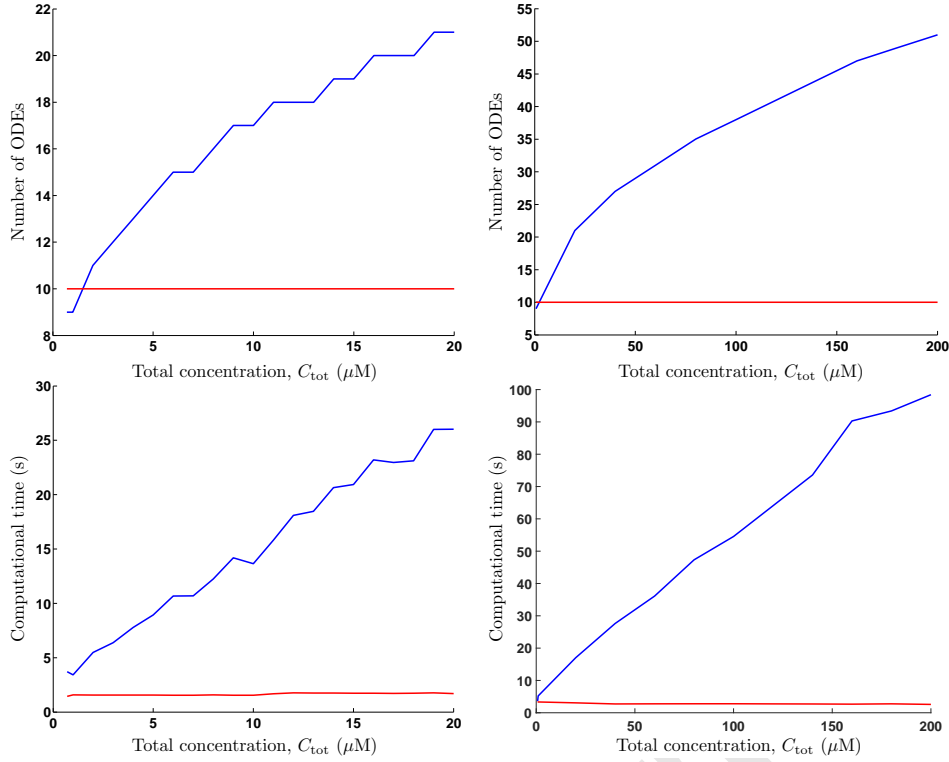


Fig. S4. The number of ODEs (top row) comprising the model (1) (blue lines) and AFM (red lines) and computational cost (bottom row) as a function of the *in vitro* (left column) and *in vivo* (right column) total concentration C_{tot} . The stopping criteria of convergence of (1) is set to $[B_N] < 10^{-4} \mu\text{M}$, where $[B_N]$ is the concentration of the largest bundle composed of N filaments.

rates associated to the lateral dissociation of two filaments, a filament and a bundle or two bundles, therefore, we redefine k_{bu}^- as follows,

$$k_{\text{bu}}^- = k_{\text{bu}}^{0-} e^{-\Delta U_b^{\text{mod}}} \begin{cases} 1 & \bar{L}_{\text{fb}}^m \leq 1 \\ e^{-(\bar{L}_{\text{fb}}^m - 1)(U_b^{\text{mod}})} & \bar{L}_{\text{fb}}^m > 1 \end{cases} \quad [\text{S20}]$$

where U_b^{mod} and ΔU_b^{mod} are the modified bond energy per lateral bond and the modified increment of lateral energy, respectively. We define U_b^{mod} as the average of the bond energies per lateral bond correspondent to the three aforementioned types of dissociation, and ΔU_b^{mod} as the average increment of lateral energies associated to the last two dissociations in a similar way that are presented for AFM in S7, i.e., $U_b^{\text{mod}} = [U_b + (U_b + \Delta U_{b,\text{ZapA}}) + (U_b + 2\Delta U_{b,\text{ZapA}})]/3$ and $\Delta U_b^{\text{mod}} = (\Delta U_{b,\text{ZapA}} + 2\Delta U_{b,\text{ZapA}})/2$.

Table S7 shows the timing predicted by the *in vivo* version of (1) in comparison to AFM predictions. Both intermediate and long kinetics predicted by (1) are not accurate; except for the attachment time of polymers to the membrane, t_{att} , the rest of the times are much shorter than the ones that have been observed experimentally.

Table S8 shows correct predictions from both models for the amount of FtsZ attached to the membrane and the average length of the polymers at the steady state. The concentration of monomers at the steady state and the number of filaments per bundles, however, are overestimated and underestimated, respectively, by (1).

The computational time required by the *in vivo* version of (1) is 64.11 – 174.74 seconds (37-61 ODEs) for the range of concentrations $C_{\text{tot},C;0} = 6 - 18 \mu\text{M}$, whereas AFM only

spends around 12 – 13 seconds (11 ODEs) regardless of the concentration, i.e., 6-14 times shorter. The average number of filaments per bundle predicted by (1) is 2-3 times lower than the number predicted by AFM and the ones estimated from the thick bundles/clusters observed experimentally. It means that the computational time would be even much larger for an improved *in vivo* version of (1) that predicted correct bundle sizes, since it would require even more ODEs.

Table S9 includes the time required by our computer, Windows 10 Home, Intel(R) Core(TM) i7-6700HQ CPU 2.60 GHz, to execute six different MATLAB tasks: LU, perform LU decomposition of a full matrix; FFT, perform fast Fourier transform of a full vector; ODE, solve van der Pol equation with ODE45 subroutine, Sparse, solve a symmetric sparse linear system; 2-D, plot Lissajous curves; and 3-D, display colormapped peaks subroutine with clipping and transforms. We have used version R2016b of MATLAB and the subroutine `bench`, that measures the execution speed of six different MATLAB tasks and compares it to the speed of several other computers. Since the majority of the calculations performed by this study have required the use of the ODE45 subroutine, we highlight the correspondent computational times to that task. As we can see, our computer is one of the fastest.

Some of the MATLAB codes developed for this study are available for download in the github repository ‘AlvaroRuiz-Martinez/ecoliproject.github’.

S5. AFM-based Description of Z-ring Formation

Physiological considerations. In *Escherichia coli* cells, the Ter linkage, a chain made of several proteins (MatP, ZapA,

Table S7. Comparison of timing predictions of FtsZ ring formation for a characteristic range of *in vivo* FtsZ concentrations, $C_{\text{tot},C;0} = 6-18 \mu\text{M}$. * denotes that the model (1) has been slightly modified by introducing *in vivo* factors.

$C_{\text{tot},C;0} (\mu\text{M})$	$t_{\text{att}} (\text{s})$		$t_{\bar{L}} (\text{s})$		$t_{\text{mon}} (\text{s})$		$t_{\bar{f}} (\text{s})$	
	(1)*	AFM	(1)*	AFM	(1)*	AFM	(1)*	AFM
6.0	19	19	26	49	37	220	31	244
12.0	11	10	13	53	22	217	19	240
18.0	8	8	15	40	32	210	24	233

Table S8. Comparison of FtsZ ring feature predictions for a characteristic range of *in vivo* FtsZ concentrations, $C_{\text{tot},C;0} = 6-18 \mu\text{M}$, at steady state ($t \rightarrow \infty$). * denotes that the model (1) has been slightly modified by introducing *in vivo* factors.

$C_{\text{tot},C;0} (\mu\text{M})$	$C_{\text{tot},\text{CM}}^{\text{a},\infty} (\mu\text{M})$		$\bar{L}_{\text{tot}}^{m,\infty}$		$C_{\text{m},\text{CM}}^{\text{d},\infty} (\mu\text{M})$		$\bar{f}_{\text{tot}}^{\infty}$	
	(1)*	AFM	(1)*	AFM	(1)*	AFM	(1)*	AFM
6.0	237	237	23.04	24.43	1.90	1.13	3.98	9.4
12.0	474	474	23.51	24.47	2.29	1.20	5.38	16.4
18.0	711	711	23.86	24.49	2.52	1.25	6.57	22.7

Table S9. MATLAB Benchmarking (times in seconds)

Computer time	LU	FFT	ODE	Sparse	2-D	3-D
Windows 7, Intel Xeon E5-1650 v3 3.50 GHz	0.1330	0.1280	0.0535	0.0968	0.2334	0.2309
iMac, OS X 10.10.5, Intel Core i7 3.4 GHz	0.1422	0.1432	0.0967	0.1120	0.3811	0.3203
Windows 10, Intel Xeon X5650 2.67 GHz	0.1422	0.1432	0.0967	0.1120	0.3811	0.3203
Linux, Intel Xeon CPU W3690 3.47 GHz	0.2027	0.1250	0.1420	0.1337	0.9327	0.7505
Windows 10 Home, Intel(R) Core(TM) i7-6700HQ CPU 2.60 GHz	0.1649	0.1363	0.0660	0.1219	1.4447	1.4613
Surface Pro 3, Windows 8.1, Intel Core i5-4300U 1.9 GHz	0.4426	0.2447	0.1256	0.2108	0.9683	0.8135
MacBook Pro, OS X 10.11.4, Intel Core i5 2.6GHz	0.2537	0.1922	0.0678	0.1212	2.2133	1.7815
Windows 8, AMD A8-6410 APU 2.00 GHz	0.9729	0.5021	0.2867	0.6188	1.5988	1.3353

and ZapB), coordinates localization of both the Z-ring and the Ter macrodomain region of the chromosome at the center of a mother cell. Once a daughter cell is born, its correspondent linkage is localized at the nucleoid periphery close to one of its poles. Then, the Ter region moves to the center of the nucleoid and promotes Z-ring formation in the middle of a cell (18–21). While this happens, FtsZ proteins in monomeric or protofilament forms diffuse in the cytoplasm. FtsA and ZipA proteins are responsible for the attachment of FtsZ to the membrane, while ZapA proteins increase the stiffness of FtsZ bundles.

Cell shape. Since our model is designed for well-mixed systems, we focus on the concentration of FtsZ proteins in a region in the middle of the cell and close to the membrane (Fig. S5). We conceptualize this region, CM, as a torus of elliptical cross-section with axial width w_a and radial width w_r , so that its volume is

$$V_{\text{CM}} = 2\pi \underbrace{\left(R - \frac{w_r}{2}\right)}_{\text{ring's length}} \underbrace{\pi \frac{w_a}{2} \frac{w_r}{2}}_{\text{ring's cross-section}} \quad [\text{S21}]$$

where R is the cell's radius. The cell of length L is composed of two semi-spherical caps, CC, and a cylindrical middle, MID, whose volumes are V_{CC} and V_{MID} , respectively (Fig. S5). Then, the cell's volume is

$$V_{\text{CELL}} = \underbrace{2 \frac{2}{3} \pi R^3}_{2 \times V_{\text{CC}}} + \underbrace{(L - 2R)\pi R^2}_{V_{\text{MID}}} \quad [\text{S22}]$$

The cell birth-growth-division process takes 20 min, with the period between Z-ring positioning in the middle and the onset of septation occurring from 4.5 min to 8.5 min after the cell's birth (22). We focus on the latter time interval, during which the cell length increases from $L \approx 2.8 \mu\text{m}$ to $\approx 3.2 \mu\text{m}$ (23). For this reason, we keep both L and R constant. Their values, as well as values of the other parameters introduced in this section, are collated in Table S10.

Table S10. Parameters of the *in vivo* model.

Parameter	Units	Value	Reference
L	μm	3	(23)
R	μm	0.4	(23)
w_a	μm	0.10	(24, 25)
w_r	μm	0.06	(25)
$C_{\text{cr, wt}}^1$	μM	1.1	(3, 13)
k_{bind}^+	$\mu\text{M}^{-1}\text{s}^{-1}$	0.142	(26)
k_{bind}^-	s^{-1}	0.0284	(26)
$[\text{FtsZ}]_{\text{C}}/[\text{FtsA}]_{\text{C}}$	–	5	(27)
$[\text{FtsZ}]_{\text{C}}/[\text{ZipA}]_{\text{C}}$	–	10	(28)
D_{CM}^{d}	$\mu\text{m}^2\text{s}^{-1}$	2.5	(12, 29)
D_{CM}^{a}	$\mu\text{m}^2\text{s}^{-1}$	0.1	(30)
Δ_{ZapA}	–	3.33	(6, 31)

Interactions between FtsZ species and the membrane. The process of monomers interacting in the cytosol to form protofilaments is not explicitly modeled in AFM. Instead, following (32), we assume that monomers and first protofilaments

diffuse in the cytosol and, upon attaching to the membrane at the midcell, they anneal and bundle to form the ring.

Let $C_{\text{tot,C};0} = N_{\text{FtsZ}}^{\text{cell}}/V_{\text{CELL}}$ denote the total cytosolic concentration of FtsZ molecules (in all forms) in the beginning of the assembly process, defined as the ratio of the total number of molecules in a cell ($N_{\text{FtsZ}}^{\text{cell}}$) to the cell volume (V_{CELL}). Let $C_{\text{tot,CM}}^{\text{a}}$ and $C_{\text{tot,CM}}^{\text{d}}$ designate the concentrations of FtsZ species (in all forms) that are respectively attached to and detached from the membrane within the CM region of the cell (Fig. S5). As FtsZ molecules attach to the membrane within the CM region, the total cytosolic concentration of detached FtsZ molecules in the cell ($C_{\text{tot,C}}$) decreases,

$$C_{\text{tot,C}} = C_{\text{tot,C};0} - C_{\text{tot,CM}}^{\text{a}} \frac{V_{\text{CM}}}{V_{\text{CELL}}}. \quad [\text{S23}]$$

This relation assumes that during the ring assembly, which takes approximately 1 min (33, 34), the cell produces no appreciable amount of new FtsZ molecules. This is a reasonable assumption, given that this time interval is a small fraction of the 20-min life cycle during which the cell doubles the initial number of FtsZ proteins for its two descendants.

Detached FtsZ molecules in the CM region are assumed to be in the form of either monomers or protofilaments, so that their total concentration $C_{\text{tot,CM}}^{\text{d}}$ is the sum of the two, $C_{\text{tot,CM}}^{\text{d}} = C_{\text{m,CM}}^{\text{d}} + C_{\text{p,CM}}^{\text{d}}$, with $C_{\text{m,CM}}^{\text{d}}$ and $C_{\text{p,CM}}^{\text{d}}$ denoting the local (within CM) concentrations of monomers and protofilaments, respectively. Henceforth, we assume that $C_{\text{tot,CM}}^{\text{d}} = C_{\text{tot,C}}$ since CM region is a subvolume of the entire cell; also $C_{\text{m,CM}}^{\text{d}} = [Z^{\text{na}}] + [Z]$, therefore, the concentration of detached protofilaments in the CM region is defined as $C_{\text{p,CM}}^{\text{d}} = C_{\text{tot,CM}}^{\text{d}} - C_{\text{m,CM}}^{\text{d}} = C_{\text{tot,CM}}^{\text{d}} - [Z^{\text{na}}] - [Z]$. Experimental evidence (35) suggests that single monomers do not attach to the membrane, while larger structures do, i.e., $C_{\text{tot,CM}}^{\text{a}} \approx C_{\text{p,CM}}^{\text{a}}$. Among the latter, FtsZ dimers are shown to be too weak (3), so that trimers are the smallest attached protofilaments in our model. The rate with which FtsZ trimers are attached to the membrane is given by

$$k_{\text{bind}}^+ \frac{C_{\text{p,CM}}^{\text{d}}}{3} (C_{\text{tot,CM}}^{\text{a,max}} - C_{\text{tot,CM}}^{\text{a}}), \quad [\text{S24}]$$

where k_{bind}^+ is a rate constant (26); and a value of the maximal concentration of FtsZ (in all forms) attached to the membrane at the midcell, $C_{\text{tot,CM}}^{\text{a,max}}$, is estimated from the following considerations.

In vivo model in (26) defined a fix number of FtsA and ZipA molecules per cell. We, however, set constant FtsZ/FtsA and FtsZ/ZipA cytosolic concentration ratios from experimental data so the number of binding sites is proportional to the FtsZ concentration. The ratio of cytosolic concentrations of FtsA and FtsZ molecules is $[\text{FtsA}]_{\text{C}}/[\text{FtsZ}]_{\text{C}} = 1/5$ (27); and the number of ZipA and FtsZ molecules in a cell are, respectively, $N_{\text{ZipA}}^{\text{cell}} = 100 - 1000$ and $N_{\text{FtsZ}}^{\text{cell}} = 5000 - 15000$ (27, 28, 36). This gives a range $[\text{ZipA}]_{\text{C}}/[\text{FtsZ}]_{\text{C}} \in [100/15000, 1000/5000] = [0.007, 0.2]$, of which we take an intermediate value $[\text{ZipA}]_{\text{C}}/[\text{FtsZ}]_{\text{C}} = 0.1$. Approximately 30% of ZipA is incorporated into the ring (37); the same percentage of FtsA is assumed in our model. Therefore, the number of

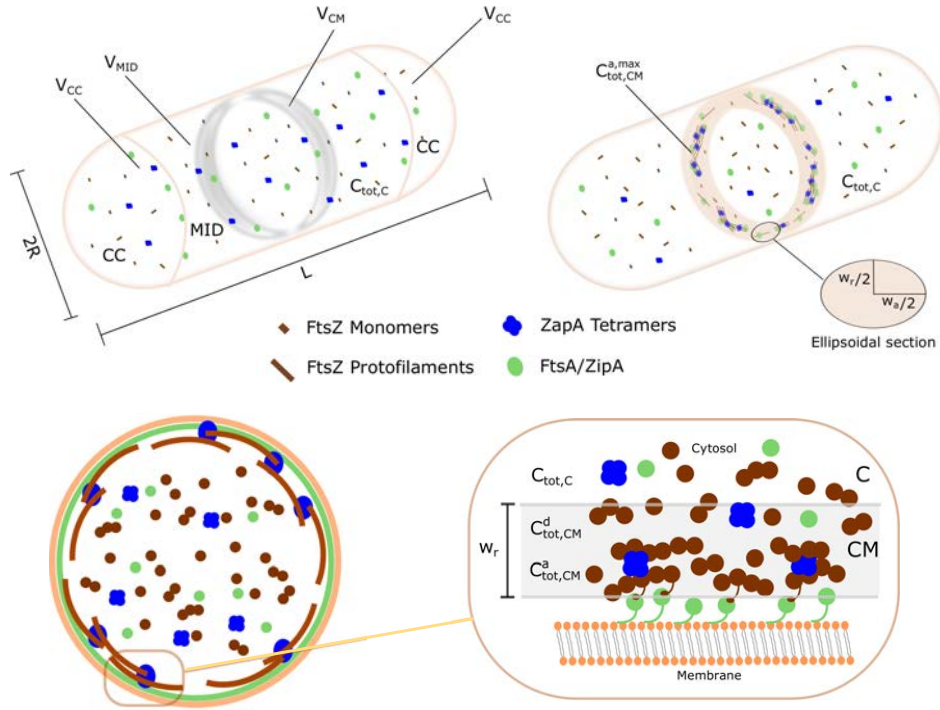


Fig. S5. Top row: *Escherichia coli* cell before (left) and after (right) ring formation. Bottom row: Cross-section of the cell (left) and a magnified region near the cell membrane (right).

binding sites in the CM region is

$$\begin{aligned}
 N_{bs} &= 0.3 ([FtsA]_C + [ZipA]_C) \frac{N_A V_{CELL}}{10^{21}} \\
 &= 0.3 \left(\frac{1}{5} C_{tot,C;0} + \frac{1}{10} C_{tot,C;0} \right) \frac{N_A V_{CELL}}{10^{21}} \\
 &= \frac{9}{100} \frac{C_{tot,C;0} N_A V_{CELL}}{10^{21}} \\
 &= \frac{9}{100} N_{FtsZ}^{cell}, \quad [S25]
 \end{aligned}$$

where N_A is Avogadro's number and $C_{tot,C;0}$ has been taken as a reference for the FtsZ/FtsA and FtsZ/ZipA ratios such that $[FtsZ]_C = C_{tot,C;0}$.

We estimate a molecule of FtsA or ZipA to include 3 – 4 FtsZ monomers. (This is consistent with an average distance, $d_{FtsA-ZipA}$, between the FtsA and ZipA molecules homogeneously distributed at the membrane in the CM region. Indeed, for a midrange value $N_{FtsZ}^{cell} = 10000$,

$$d_{FtsA-ZipA} = \sqrt{\frac{\text{Midcell area}}{N_{bs}}} = \sqrt{\frac{2\pi R w_a}{N_{bs}}} = 16.7 \text{ nm}, \quad [S26]$$

which corresponds to the length of a FtsZ protofilament made of 3 – 4 monomers of 5 nm diameter per monomer.) Taking the midrange value of 3.5 FtsZ monomers per molecule of FtsA or ZipA, the maximal concentration of FtsZ (in all forms) attached to the membrane at the midcell is

$$C_{tot,CM}^{a,max} = 3.5 \frac{N_{bs}}{V_{CM}} \frac{10^{21}}{N_A} \approx 0.315 \frac{V_{CELL}}{V_{CM}} C_{tot,C;0}. \quad [S27]$$

This estimate is in agreement with an estimate that 30 – 35% of total FtsZ is incorporated into the ring (37, 38).

Finally, we allow the shortest and weakest protofilaments, i.e., dimers, to detach at the rate

$$k_{bind}^- [Z_2]. \quad [S28]$$

Bundling. The FtsZ assembly process in wild-type cells remains unknown. However, there are numerous of *in vitro* and *in vivo* studies that show filaments forming bundles and more complex structures (4, 31, 39–42). Following a recent *in vivo* study (25), which suggests a heterogeneous and discontinuous three-dimensional ring structure made of FtsZ clusters, we propose a two-stages bundling process:

1. FtsZ filaments, F , and first bundles, B_2 and B_3 , associate laterally to form two-dimensional sheets upon attaching to the membrane, as observed *in vitro* (4, 43) and *in vivo* (44). Wider bundles, B_w , grow in axial direction as long as the concentration of FtsZ proteins at the membrane, $C_{tot,CM}^a$, increases. They are also allowed to grow in radial direction by pushing and lifting each other from the membrane. That results in formation of bundles partially attached to the membrane with more degrees of freedom to rearrange into three-dimensional cross-linked clusters along the CM region.
2. In the second stage, all binding sites at the membrane are occupied by FtsZ proteins and there is not much space for wide bundles to grow in two dimensions. Wide bundles only form three-dimensional cross-linked clusters.

ODEs for *in vivo* systems. *In vivo* polymerization and bundling processes are represented by the following ODEs. Concentrations in the CM region, *in vivo* reaction rates, and parameters θ and χ are defined in this Section. Section S7 includes information about *in vivo* bundling rates.

$$\begin{aligned} \frac{d[Z^{\text{na}}]}{dt} = & -k_{\text{ac}}^+[Z^{\text{na}}] + k_{\text{ac}}^-[Z] + k_{\text{hy/dis}}^1[F] + \\ & k_{\text{hy/dis}}^2 \left([F] + \sum_{i=2}^3 [B_i] \right) + \\ & k_{\text{hy/dis}}^3 \left(\sum_{i=2}^3 [B_i] + [B_w] \right), \end{aligned} \quad [\text{S29}]$$

$$\begin{aligned} \frac{d[Z]}{dt} = & k_{\text{ac}}^+[Z^{\text{na}}] - k_{\text{ac}}^-[Z] - 2k_{\text{nu}}^+[Z]^2 + 2k_{\text{nu}}^-[Z_2] - \\ & k_{\text{el}}^+[Z] \sum_{i=2}^3 [Z_i] - k_{\text{el}}^+[Z][F] + k_{\text{el}}^-[Z_3] \\ & + k_{\text{el}}^-[F] - k_{\text{mb}}[Z] \left(\sum_{i=2}^3 [B_i] + [B_w] \right), \end{aligned} \quad [\text{S30}]$$

$$\frac{d[Z_2]}{dt} = k_{\text{nu}}^+[Z]^2 - k_{\text{nu}}^-[Z_2] - k_{\text{el}}^+[Z][Z_2] + k_{\text{el}}^-[Z_3] - k_{\text{bind}}^-[Z_2], \quad [\text{S31}]$$

$$\begin{aligned} \frac{d[Z_3]}{dt} = & k_{\text{el}}^+[Z]([Z_2] - [Z_3]) - k_{\text{el}}^-[Z_3] + \\ & \frac{1}{3}k_{\text{bind}}^+C_{\text{p,CM}}^{\text{d}}(C_{\text{tot,CM}}^{\text{a,max}} - C_{\text{tot,CM}}^{\text{a}}), \end{aligned} \quad [\text{S32}]$$

$$\begin{aligned} \frac{d[F]}{dt} = & k_{\text{el}}^+[Z][Z_3] - k_{\text{an}}^+[F]^2 + k_{\text{an}}^-[F] - \\ & k_{\text{bu}}^+[F] \left(2\theta[F] + \theta \sum_{i=2}^3 [B_i] + \chi[B_w] \right) + \\ & k_{\text{bu}}^- (2[B_2] + [B_3] + [B_w]) + k_{\text{hy/dis}}^2[F], \end{aligned} \quad [\text{S33}]$$

$$\frac{d[B_2]}{dt} = k_{\text{bu}}^-([B_3] - [B_2]) + \theta k_{\text{bu}}^+[F]([F] - [B_2]) + k_{\text{hy/dis}}^2[B_2], \quad [\text{S34}]$$

$$\frac{d[B_3]}{dt} = -k_{\text{bu}}^-[B_3] + \theta k_{\text{bu}}^+[F]([B_2] - [B_3]) + k_{\text{hy/dis}}^2[B_3], \quad [\text{S35}]$$

$$\frac{d[B_w]}{dt} = \theta k_{\text{bu}}^+[F][B_3] - \chi k_{\text{bu}}^+[B_w]^2 + k_{\text{bu}}^-[B_w]. \quad [\text{S36}]$$

We also define ODEs for the concentration of monomers in long filaments and bundles attached to the membrane, $C_{\text{fb,CM}}^{m,a}$, and the concentration of filaments in wide bundles at the membrane, $C_{\text{wb,CM}}^{f,a}$,

$$\begin{aligned} \frac{dC_{\text{fb,CM}}^{m,a}}{dt} = & 4k_{\text{el}}^+[Z][Z_3] + k_{\text{el}}^+[Z][F] - k_{\text{el}}^-[F] - k_{\text{hy/dis}}^1[F] - \\ & k_{\text{hy/dis}}^2 \left([F] + \sum_{i=2}^3 [B_i] \right) \\ & - k_{\text{hy/dis}}^3 \left(\sum_{i=2}^3 [B_i] + [B_w] \right) + \\ & k_{\text{mb}}[Z] \left(\sum_{i=2}^3 [B_i] + [B_w] \right), \end{aligned} \quad [\text{S37}]$$

$$\frac{dC_{\text{wb,CM}}^{f,a}}{dt} = 4\theta k_{\text{bu}}^+[F][B_3] - k_{\text{bu}}^-[B_w] + \chi k_{\text{bu}}^+[F][B_w]. \quad [\text{S38}]$$

Finally, the ODE for the concentration of FtsZ in polymer form attached to the membrane is defined as follows,

$$\begin{aligned} \frac{dC_{\text{tot,CM}}^{\text{a}}}{dt} = & 2k_{\text{nu}}^+[Z]^2 - 2k_{\text{nu}}^-[Z_2] + k_{\text{el}}^+[Z] \left(\sum_{i=2}^3 [Z_i] + [F] \right) - \\ & k_{\text{el}}^-([Z_3] + [F]) - k_{\text{hy/dis}}^1[F] - \\ & k_{\text{hy/dis}}^2 \left([F] + \sum_{i=2}^3 [B_i] \right) \\ & - k_{\text{hy/dis}}^3 \left(\sum_{i=2}^3 [B_i] + [B_w] \right) + \\ & k_{\text{mb}}[Z] \left(\sum_{i=2}^3 [B_i] + [B_w] \right) + \\ & k_{\text{bind}}^+C_{\text{p,CM}}^{\text{d}}(C_{\text{tot,CM}}^{\text{a,max}} - C_{\text{tot,CM}}^{\text{a}}) - 2k_{\text{bind}}^-[Z_2]. \end{aligned} \quad [\text{S39}]$$

Eqs. S29–S39 are subject to initial conditions $[Z^{\text{na}}]_0 = C_{\text{m,CM};0}^{\text{d}}$, $[Z]_0 = 0$, $[Z_i]_0 = 0$, $[F]_0 = 0$, $[B_i]_0 = 0$, $[B_w]_0 = 0$, $C_{\text{fb,CM};0}^{m,a} = 0$, $C_{\text{wb,CM};0}^{f,a} = 0$ and $C_{\text{tot,CM};0}^{\text{a}} = 0$, with $i = 2, 3$.

The system of 11 ODEs is solved with ODE15s Matlab function for stiff problems. It is a variable-step, variable-order (VSVO) solver based on the numerical differentiation formulas (NDFs) of orders 1 to 5.

Model parametrization.

First critical concentration. An experimentally determined range of the first critical concentration for FtsZ mutants, $C_{\text{cr,mut}}^1 = 0.1 - 0.7 \mu\text{M}$ (the majority of mutants from (13)) and the mutant from (3), is lower than the values observed in wild-type FtsZ proteins, $C_{\text{cr,wt}}^1 = 0.9 - 1.25 \mu\text{M}$ (13, 45). In our model of *in vivo* wild-type FtsZ assembly, we take an intermediate value in the latter range, $C_{\text{cr,wt}}^1 = 1.1 \mu\text{M}$, instead of the value $C_{\text{cr}}^1 = 0.7 \mu\text{M}$ used in our model of the mutant FtsZ-F268C.

Bundling. In both stages of the bundling process described above, ZapA tetramers contribute to increase the size and the rigidity of the two-dimensional sheets and the three-dimensional cross-linked clusters. Section S7 shows the influence of these structural changes on the forward and backward bundling rates.

Crowding at the membrane increases reaction rates of a reaction-limited bundling, i.e., when proteins are small and crowding favors protein-protein association; on the other hand, crowding reduces reaction rates once the bundling reaction becomes diffusion-limited, i.e., when molecules are large (46). As in the case of *in vitro* polymerization, we treat bundling as a diffusion-limited reaction. Thus, the bundling reaction rate is reduced by a concentration-dependent factor θ that is defined as

$$\theta = 1 + (\chi - 1) \frac{C_{\text{tot,CM}}^{\text{a}}}{C_{\text{tot,CM}}^{\text{a,max}}}, \quad [\text{S40}]$$

where $\chi = D_{\text{CM}}^{\text{a}}/D_{\text{CM}}^{\text{d}}$ is the ratio of the diffusion of the species attached to crowded membranes to the diffusion of the ones

that are not attached (see Table S10). In the beginning of the assembly process, the concentration of polymers attached to the membrane is $C_{\text{tot,CM}}^a = 0$. The factor θ reaches its maximum value, $\theta = 1$, in the absence of crowding effects, i.e., FtsZ species bundle at the maximal rates. Once all binding sites are occupied by FtsZ species, the CM region becomes completely crowded such that $C_{\text{tot,CM}}^a = C_{\text{tot,CM}}^{a,\text{max}}$ and θ reaches its minimum value, $\theta = \chi$.

As in the *in vitro* case, wide bundles, B_w , are relevant at long times and high concentrations. Thus, we set $\theta = \chi$ for any forward bundling reaction with B_w as a reactant.

Hydrolysis/dissociation rates. Dissociation upon hydrolysis rates are redefined for the CM region as

$$\begin{aligned} k_{\text{hy/dis}}^i &= k_{\text{hss/dis}}^i \frac{C_{\text{tot,CM}}^a + C_{\text{tot,CM}}^d - [Z^{\text{na}}] - [Z]}{C_{\text{tot,CM}}^a + C_{\text{tot,CM}}^d - C_{\text{cr,wt}}^1} \\ &= k_{\text{hss/dis}}^i \frac{C_{\text{tot,CM}}^a + C_{\text{tot,C}} - [Z^{\text{na}}] - [Z]}{C_{\text{tot,CM}}^a + C_{\text{tot,C}} - C_{\text{cr,wt}}^1} \end{aligned} \quad [\text{S41}]$$

for $i = 1, 2, 3$.

ZapA deficiency. Lack of ZapA proteins introduces five modifications in our model.

1. The absence of ZapA alters the chain of molecules that compose the terminal Ter, therefore, we assume that FtsZ attach to the whole membrane rather than its CM part. Consequently, we redefine the CM region as a thin volume of radial width $w_r = 20$ nm along the entire cell,

$$V_{\text{CM}} = 2\pi \left(R - \frac{w_r}{2}\right) (L - 2R) w_r + 4\pi \left(R - \frac{w_r}{2}\right)^2 w_r. \quad [\text{S42}]$$

2. The percentage of FtsA and ZipA at the membrane is assumed to be 100% instead of 30%.
3. The average number of filament per bundle is computed with Eq. S14b.
4. The stiffness of FtsZ bundles is not altered by ZapA, so that $\Delta_{\text{ZapA}} = 1$.
5. An estimated average length for wide bundles is assumed to equal the maximum length predicted by our *in vitro* model at high concentrations. We base this assumption on the facts that concentrations at the membrane are higher than *in vitro* concentrations and also that there are no ZapA proteins to stabilize longitudinal bonds. Consequently, we set $\bar{L}_{\text{fb}}^m = 35$ in the backward bundling rate applied to wide bundles in Section S7.

S6. *In vitro* bundling reactions and their rates

Forward bundling rate. A general forward bundling reaction can be defined as



where R_1 and R_2 denote two linear chain molecules diffusing and binding laterally in order to produce the species P . If bundling is a diffusion-limited process, then Smoluchowski's formula,

$$k_{\text{bu}}^+ = 4\pi(D_{R_1} + D_{R_2})(r_{\text{h},R_1} + r_{\text{h},R_2}), \quad [\text{S44}]$$

enables one to express the bundling rate k_{bu}^+ in terms of the diffusion coefficients, D_{R_1} and D_{R_2} , and the hydraulic radii, r_{h,R_1} and r_{h,R_2} , of the reactants R_1 and R_2 .

To estimate values of D_{R_i} ($i = 1, 2$), we deploy the Rouse model that treats a short unentangled polymer as a linear series of n beads connected by springs with negligible hydrodynamic interactions (47). This description is applicable to polymers with a number of beads smaller than a characteristic entanglement length, $n_e \approx 35$ (48). Treating each monomer as a ‘‘bead’’, the number of beads in a filament or bundle is given by the latter's average length, i.e., $n = \bar{L}_{\text{fb}}^m$. The Rouse model is applicable to the experiments (3), since the observed average length of FtsZ species is $\bar{L}_{\text{fb}}^m < 30$. Thus, if reactants R_i ($i = 1, 2$) represent FtsZ filaments (F) and/or bundles (B_2 , B_3 and B_w), their diffusion coefficient is

$$D_{R_i} = \frac{k_B T}{\bar{L}_{\text{fb}}^m \zeta_{\text{bead},R_i}}, \quad i = 1, 2. \quad [\text{S45}]$$

Here k_B is the Boltzmann constant, T is room temperature, and ζ_{bead,R_i} is the friction coefficient of a bead. For a non-spherical molecule (bead) in a solvent of viscosity η_s ,

$$\zeta_{\text{bead},R_i} = 6\pi\eta_s r_{\text{bead},R_i}^s F_{\text{bead},R_i}, \quad i = 1, 2, \quad [\text{S46}]$$

where r_{bead,R_i}^s is the radius of a sphere whose volume equals that of the bead, and F_{bead,R_i} is the Perrin factor (or translational shape factor) defined as the ratio of the friction coefficient of a non-spherical molecule to that of a spherical molecule of the same volume (49). The volume of a spherical monomer of radius r_m is $V = 4\pi r_m^3/3$. The volume of a bead comprising a filament or bundle, R_i , with average number of filaments f_{R_i} is

$$V_{\text{bead},R_i} = \bar{f}_{R_i} \frac{4\pi}{3} r_m^3. \quad [\text{S47}]$$

An equivalent spherical bead of the same volume, V_{bead,R_i} , has the radius

$$r_{\text{bead},R_i}^s = \sqrt[3]{\bar{f}_{R_i} r_m}. \quad [\text{S48}]$$

For filaments and bundles R_i with cylindrical shapes, the beads are disks of thickness $2r_m$ and volume $V_{\text{bead},R_i}^d = 2\pi r_m (r_{\text{bead},R_i}^d)^2$ (see Figure S6 in which the bundle is composed of 9 filaments). This volume equals that in Eq. S47 if the disk-shaped bead has a radius

$$r_{\text{bead},R_i}^d = \sqrt{\frac{2}{3} \bar{f}_{R_i} r_m}. \quad [\text{S49}]$$

The Perrin factor for a disk of thickness $2r_m$ and diameter $2r_{\text{bead},R_i}^d$ is (50)

$$F_{\text{bead},R_i} = \sum_{k=0}^7 a_k x_{R_i}^k, \quad x_{R_i} = \ln p_{R_i}, \quad p_{R_i} = \frac{r_m}{r_{\text{bead},R_i}^d}, \quad [\text{S50}]$$

where $a_0 = 1.0304$, $a_1 = 0.0193$, $a_2 = 0.06229$, $a_3 = 0.00476$, $a_4 = 0.00166$, $a_5 = a_6 = 0$, and $a_7 = 2.66 \times 10^{-6}$. This polynomial representation is valid on the range $p_{R_i} \in [0.01, 100]$. Substituting Eq. S49 into Eq. S50 yields $p_{R_i}^2 = 3/(2\bar{f}_{R_i})$ and defines the applicability range for the Rouse model as $\bar{f}_{R_i} \in [1.5 \times 10^{-4}, 1.5 \times 10^4]$. This is not overly restrictive,

since $\bar{f}_{R_i} < 1.5 \times 10^{-4}$ is equivalent to the absence of filaments and bundles, and $\bar{f}_{R_i} > 1.5 \times 10^4$ is not observed in the experiments (3). Substituting Eqs. S46, S48 and S50 into Eq. S45 gives the Rouse diffusion coefficient for reactant R_i ,

$$D_{R_i} = \frac{A}{\bar{L}_{fb}^m \sqrt[3]{\bar{f}_{R_i} F_{bead,R_i}(\bar{f}_{R_i})}}. \quad [S51]$$

where A is a computable constant.

The hydrodynamic radius of a chain of n molecules of radius r_m is proportional to $r_m n^\nu$, where

$$\nu = \begin{cases} 3/(d+2) & d \leq 4 \\ 1/2 & d > 4 \end{cases} \quad [S52]$$

is referred to as the Flory exponent, a scaling factor for the average end-to-end distance of the polymer introduced to consider polymer self-avoidance effects, and d is a dimensionality factor. When $d \leq 1/2$, polymers are represented by a d -dimensional sphere (line, circle, sphere for $d = 1, 2, 3$) filled with n polymer segments with mutual repulsive interaction; $d > 4$ corresponds to a particular case in which ‘‘real polymer chains’’ behave as if they were ideal, i.e. excluded volume effects are negligible (47, 51, 52). We set $d = 1$, which corresponds to a one-dimensional self-avoiding walk, i.e. a straight line with length n (51). The following reasons justify this choice. First, FtsZ protofilaments and short filaments are usually straight when GTP nucleotides are dominant in the structure (40). Second, our filaments and bundles are relatively short, $\bar{L}_{fb}^m \leq 30$, and bundles get stiffer as they get wider (6). The resulting FtsZ species are, approximately, straight three-dimensional cylindrical structures, as that shown in Figure S6. Setting $d = 1$ and, hence, $\nu = 1$ translates into the hydrodynamic radius of reactant R_i ,

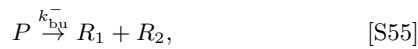
$$r_{h,R_i} \propto r_m \bar{L}_{fb}^m. \quad [S53]$$

Combining Eqs. S51, S53 and S44 leads to

$$k_{bu}^+ = M^+ \sum_{i=1}^2 \frac{1}{\sqrt[3]{\bar{f}_{R_i} F_{bead,R_i}(\bar{f}_{R_i})}}, \quad [S54]$$

where $M^+ = k_{bu}^+ F_{bead,F}(\bar{f}_F)/2$, and k_{bu}^+ is the lateral association rate of two filaments.

Backward bundling rate. In a generic backward bundling reaction,



a linear chain molecule P divides laterally into two thinner chain molecules R_1 and R_2 . Following (5), we pursue an approach based on the energetic balance of lateral fragmentation of bundles. Let k_{bu}^{0-} denote the rate of lateral detachment of two monomers, and U_b designate the lateral interaction energy of two laterally-bound monomers. In analogy to Eq. S15 for the longitudinal detachment of filaments, the dissociation rates for the bonds at the lateral tip and in the middle of bundles of one monomer long are, respectively,

$$k_{bu}^{0-} e^{-\Delta U_b} \quad \text{and} \quad k_{bu}^{0-} e^{-2\Delta U_b}, \quad [S56]$$

where ΔU_b is the increment in the energy of a laterally connected monomer. In analogy to the backward rates for nucleation, elongation and annealing of bundles (5), we define the bundling backward rates for filament-filament,

$$k_{bu}^{0-} e^{-(\bar{L}_{fb}^m - 1)U_b}, \quad [S57a]$$

filament-bundle,

$$k_{bu}^{0-} e^{-(\bar{L}_{fb}^m - 1)(U_b + \Delta U_b) - \Delta U_b} \quad [S57b]$$

and bundle-bundle,

$$k_{bu}^{0-} e^{-\sqrt{2\bar{f}_P/3}[(\bar{L}_{fb}^m - 1)(U_b + 2\Delta U_b) + 2\Delta U_b]}. \quad [S57c]$$

Here \bar{f}_P is the average number of filaments in the product P ; and the factor $\sqrt{2\bar{f}_P/3}$ represents the ratio of the radii of the product P and the filament, as defined in Eq. S49. For our kinetics model of bundling, we define bundling reaction backward rates as follows.

1. If a bundle of two filaments of average length \bar{L}_{fb}^m dissociates laterally to form two independent filaments, i.e., if $P = B_2$, then

$$k_{bu}^- = k_{bu}^{0-} \begin{cases} 1 & \bar{L}_{fb}^m \leq 1 \\ e^{-(\bar{L}_{fb}^m - 1)U_b} & \bar{L}_{fb}^m > 1. \end{cases} \quad [S58]$$

2. If a bundle of three filaments of average length \bar{L}_{fb}^m dissociates laterally to form a filament and a bundle, i.e., if $P = B_3$, then

$$k_{bu}^- = k_{bu}^{0-} e^{-\Delta U_b} \begin{cases} 1 & \bar{L}_{fb}^m \leq 1 \\ e^{-(\bar{L}_{fb}^m - 1)(U_b + \Delta U_b)} & \bar{L}_{fb}^m > 1. \end{cases} \quad [S59]$$

3. Wide bundles are mainly present at long times and high concentrations, wherein the experimentally observed average length is in the range of 24 – 30 monomers (3). We pick an intermediate value of $\bar{L}_{fb}^m = 27$. Thus, if a wide bundle, with average number of filaments \bar{f}_{wb} and average length \bar{L}_{fb}^m , dissociates laterally to form a filament and another bundle, i.e., if $P = B_w$, $R_1 = F$ and $R_2 = B_w$, then

$$k_{bu}^- = k_{bu}^{0-} e^{-26(U_b + \Delta U_b) - \Delta U_b}. \quad [S60]$$

Wide bundles exist, and hence this dissociation reaction takes place and Eq. S60 is applicable, when $1.5 \times 10^{-4} \leq \bar{f}_{wb} \leq 1.5 \times 10^4$ (see the preceding section). If $\bar{f}_{wb} < 1.5 \times 10^{-4}$, then this reaction is absent so that its rate is $k_{bu}^- = 0$.

4. If a wide bundle, with average number of filaments \bar{f}_{wb} and average length $\bar{L}_{fb}^m = 27$, dissociates laterally to form two bundles, i.e., if $P = B_w$, $R_1 = B_w$ and $R_2 = B_w$, then

$$k_{bu}^- = k_{bu}^{0-} e^{-\sqrt{2\bar{f}_{wb}/3}[26(U_b + 2\Delta U_b) + 2\Delta U_b]}. \quad [S61]$$

This expression holds for $1.5 \times 10^{-4} \leq \bar{f}_{wb} \leq 1.5 \times 10^4$; if $\bar{f}_{wb} < 1.5 \times 10^{-4}$, then $k_{bu}^- = 0$.

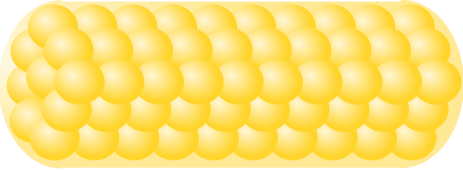
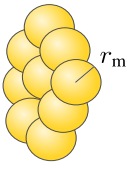
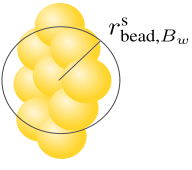
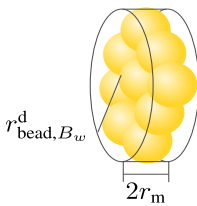
BUNDLE	Bead	Bead as a sphere	Bead as a disk
			
Bead dimensions	r_m	r_{bead, B_w}^s	$r_{\text{bead}, B_w}^d, 2r_m$
Bead volume	$V_{\text{bead}, B_w} = 9\frac{4}{3}\pi r_m^3$	$V_{\text{bead}, B_w}^s = \frac{4}{3}\pi (r_{\text{bead}, B_w}^s)^3$	$V_{\text{bead}, B_w}^d = 2r_m\pi (r_{\text{bead}, B_w}^d)^2$

Fig. S6. Alternative representations of a bead in a wide bundle of average width $\bar{f}_{wb} = 9$.

For the values of U_b and ΔU_b reported in Table S1, and for $\bar{f}_{wb} = 4$ associated with case 4 above, Eq. S61 gives an order-of-magnitude estimate

$$k_{\text{bu}}^- \sim \mathcal{O}(10^{-5}) \quad \text{for reaction 4.} \quad [\text{S62}]$$

Among the remaining three cases previously defined, case 3 is the least energetically favorable; even for that case, an order-of-magnitude analysis of Eq. S60 results in

$$k_{\text{bu}}^- \sim \mathcal{O}(10^{-3}) \quad \text{for reaction 3.} \quad [\text{S63}]$$

Hence, the backward bundling rate for case 4 is negligible relative to any other cases, i.e., case 4, or reaction $2B_{w;b-} \rightarrow B_{w;b+}$, is assumed to be irreversible.

S7. *In vivo* bundling reactions and their rates

In regions adjacent to membranes, we redefine bundles as two-dimensional sheets of cylindrical beads. Overlapped bundles rearrange to form three-dimensional cross-linked clusters along the CM region, which we conceptualize as long, thick structures composed of big spherical beads.

Forward bundling rate. The presence of ZapA proteins between FtsZ filaments changes a diffusion coefficient of bundles and, consequently, diffusion-limited reaction rates. Guided by the *in vitro* observations (53), we consider structures with a pair of FtsZ filaments connected by ZapA tetramers, and assume that both ZapA and FtsZ monomers have the same diameter, $\phi_m \approx 5$ nm. We allow these ZapA tetramers to diffuse like the pair of filaments. Table S11 provides discrete values of the average number of filaments of a reactant R_i without (\bar{f}_{R_i}) and with ($\bar{f}_{R_i, \text{ZapA}}$) ZapA in between pairs of FtsZ filaments.

Geometric considerations give $\bar{f}_{R_i, \text{ZapA}} = 2\bar{f}_{R_i}$ for bundles of more than two filaments. Consequently, we redefine Eq. S14b as

$$\bar{f}_{R_i, \text{ZapA}} = \begin{cases} 1 & \text{for } R_i = F \\ 2 & \text{for } R_i = B_2 \\ 6 & \text{for } R_i = B_3 \\ \bar{f}_{wb, \text{ZapA}} & \text{for } R_i = B_w, \end{cases} \quad [\text{S64}]$$

where $\bar{f}_{wb, \text{ZapA}} = 2\bar{f}_{wb}$. Now, we define a dimensionality factor \bar{d} that corresponds to a subsequent bundling stage: $\bar{d} = 2$ for bundling over the membrane, and $\bar{d} = 3$ for bundling over and

perpendicular to the membrane. For each \bar{d} , we redefine the radius of the spherical beads and the Perrin factor as follows.

For $\bar{d} = 2$, bundles are distributed along a two dimensional membrane as sheets (Fig. S7). The radius of a spherical bead is defined as

$$r_{\text{bead}, R_i}^{s(2)} = r_m \sqrt[3]{\bar{f}_{R_i, \text{ZapA}}} \quad [\text{S65}]$$

by equating volumes of a bead and its spherical counterpart,

$$V_{\text{bead}, R_i} = \bar{f}_{R_i, \text{ZapA}} \frac{4\pi}{3} r_m^3, \quad V_{\text{bead}, R_i}^s = \frac{4\pi}{3} [r_{\text{bead}, R_i}^{s(2)}]^3. \quad [\text{S66}]$$

The Perrin factor $F_{\text{bead}, R_i, \text{ZapA}}^{(2)}$ in Eq. S50 is now computed for $p_{R_i} = l_{\text{bead}, R_i}^c / \phi_{\text{bead}, R_i}^c$, where l_{bead, R_i}^c and $\phi_{\text{bead}, R_i}^c$ are respectively the length and diameter of the bead. Since $l_{\text{bead}, R_i}^c = \bar{f}_{R_i, \text{ZapA}} \phi_m$ and $\phi_{\text{bead}, R_i}^c = \phi_m$, we have $p_{R_i} = \bar{f}_{R_i, \text{ZapA}}$. The Perrin factor expression for a cylinder (50), restricts values of $\bar{f}_{R_i, \text{ZapA}}$ to the interval [0.01,100]. This constraint is always satisfied for *in vivo* cases:

1. $\bar{f}_{R_i, \text{ZapA}}$ only changes in time for wide bundles, i.e., when $R_i = B_w$. Our *in vitro* model predicts $\bar{f}_{wb} > 0.01$ for $C_{\text{tot}} = 4 - 6 \mu\text{M}$, which are the lowest cytosolic concentrations observed experimentally (3000-5000 FtsZ molecules). Since concentrations are much higher at the membrane than in the cytosol, and ZapA proteins (absent in the *in vitro* experiment) promote bundling, $\bar{f}_{wb, \text{ZapA}}^{\text{in vivo}} \gg \bar{f}_{wb}^{\text{in vitro}} > 0.01$ for $C_{\text{tot}, C} > 4 \mu\text{M}$.
2. The maximal axial width of the CM region is $w_a = 100$ nm (Table S10). For monomer diameter $\phi_m \approx 5$ nm, the maximal number of FtsZ/ZapA filaments laterally associated and perfectly aligned is 20. Thus, $\bar{f}_{wb, \text{ZapA}}^{\text{max}} = 20 < 100$ for any cytosolic concentration, $C_{\text{tot}, C}$.

For $\bar{d} = 3$, bundles are partially attached to the membrane and distributed along the midcell region as long cross-linked bundles with more complex beads. Figure S8 shows an example of beads of three-dimensional wide bundles; the bead's length (three monomers long in the longitudinal direction) is proportional to the number of cross-linked bundles. The radius of a spherical bead is

$$r_{\text{bead}, R_i}^{s(3)} = r_m \sqrt[3]{\bar{f}_{R_i, \text{ZapA}}} \quad [\text{S67}]$$

Table S11. Average number of filaments in a reactant R_i without and with ZapA proteins.

\bar{f}_{R_i}	$\bar{f}_{R_i, \text{ZapA}}$	Scheme
2	4	$(\text{ZapA})_2 - (\text{FtsZ})_2 - (\text{ZapA})_2$
4	8	$(\text{FtsZ}) - (\text{ZapA})_2 - (\text{FtsZ})_2 - (\text{ZapA})_2 - (\text{FtsZ})$
6	12	$(\text{FtsZ}) - (\text{ZapA})_2 - (\text{FtsZ})_2 - (\text{ZapA})_2 - (\text{FtsZ})_2 - (\text{ZapA})_2 - (\text{FtsZ})$
..

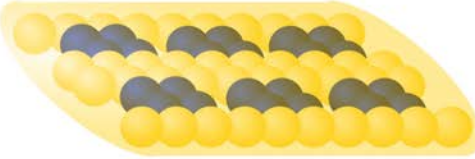
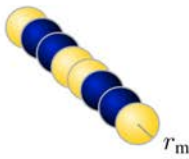
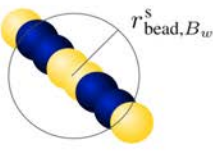
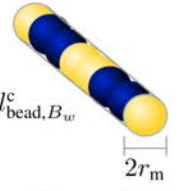
BUNDLE	Bead	Bead as a sphere	Bead as a cylinder
			
Bead dimensions	r_m	r_{bead, B_w}^s	$l_{\text{bead}, B_w}^c, 2r_m$
Bead volume	$V_{\text{bead}, B_w} = \bar{f}_{\text{wb}, \text{ZapA}} \frac{4}{3} \pi r_m^3$	$V_{\text{bead}, B_w}^s = \frac{4}{3} \pi (r_{\text{bead}, B_w}^s)^3$	$V_{\text{bead}, B_w}^c = l_{\text{bead}, B_w}^c \pi r_m^2$

Fig. S7. Graphical representations of a bead in a two-dimensional wide bundle of $\bar{f}_{\text{wb}, \text{ZapA}} = 8$.

which is obtained by equating volumes of a bead and its spherical representation,

$$V_{\text{bead}, R_i} = \bar{f}_{R_i, \text{ZapA}} \frac{4\pi}{3} r_m^3, \quad V_{\text{bead}, R_i}^s = \frac{4\pi}{3} [r_{\text{bead}, R_i}^{s(3)}]^3. \quad [\text{S68}]$$

The Rouse model's condition for the number of beads to be smaller than the entanglement length limit, $n < n_e$, is still fulfilled. The length of the beads is taken proportional to the number of cross-linked bundles connected longitudinally. Furthermore, for $\tilde{d} = 3$, the Perrin factor is defined for spheres, i.e., $F_{\text{bead}, R_i, \text{ZapA}}^{(3)} = 1$,

The hydrodynamic radius r_{h, R_i} is computed with Eq. S53. This yields an expression for the forward reaction rate,

$$k_{\text{bu}}^+ = \tilde{k}_{\text{bu}}^{0+} \sum_{i=1}^2 \sum_{\tilde{d}=2}^3 \frac{\gamma_{R_i}^{(\tilde{d})}}{\sqrt[3]{\bar{f}_{R_i, \text{ZapA}} F_{\text{bead}, R_i, \text{ZapA}}^{(\tilde{d})} (\bar{f}_{R_i, \text{ZapA})}}}, \quad [\text{S69}]$$

where

$$\tilde{k}_{\text{bu}}^{0+} = \frac{1}{2} k_{\text{bu}}^{0+} F_{F, \text{ZapA}}^{(2)} (\bar{f}_{F, \text{ZapA}}), \quad [\text{S70}]$$

$$\gamma_{R_i}^{(\tilde{d})} = \begin{cases} 1 & \tilde{d} = 2 \\ 0 & \tilde{d} = 3 \end{cases} \quad \text{if } R_i = F, B_2, \text{ or } B_3 \quad [\text{S71a}]$$

and

$$\gamma_{R_i}^{(\tilde{d})} = \begin{cases} 1 - \frac{C_{\text{tot}, \text{CM}}^a}{C_{\text{tot}, \text{CM}}^{a, \text{max}}} & \tilde{d} = 2 \quad (\bar{f}_{\text{wb}, \text{ZapA}} \leq 20) \\ \frac{C_{\text{tot}, \text{CM}}^a}{C_{\text{tot}, \text{CM}}^{a, \text{max}}} & \tilde{d} = 3 \quad (\bar{f}_{\text{wb}, \text{ZapA}} > 20) \end{cases} \quad \text{if } R_i = B_w. \quad [\text{S71b}]$$

First species in the bundling process, F , B_2 and B_3 , are assumed to grow exclusively over the membrane. The amount

of wide bundles growing over the membrane decreases as the total FtsZ concentration at the membrane, $C_{\text{tot}, \text{CM}}^a$, increases, i.e., as the membrane gets crowded and there is less space for bundles to diffuse and grow in two dimensions. On the other hand, the amount of wide bundles growing in all directions and forming cross-linked structures increases with the total FtsZ concentration at the membrane, i.e., when the membrane gets crowded and bundles push and lift each other to rearrange in three dimensions. When $C_{\text{tot}, \text{CM}}^a = C_{\text{tot}, \text{CM}}^{a, \text{max}}$, bundles grow exclusively in three dimensions.

Backward bundling rate. Local concentration of ZapA interacting stoichiometrically with FtsZ at the division site may be sufficient to induce a tetrameric conformation (54, 55). Some studies (53, 54, 56) suggest the stoichiometry of ZapA-FtsZ interaction to be 1:1, while others (31, 57) estimated stoichiometries up to 4:1 since ZapA concentration in the ring is four times higher than FtsZ concentration (31). Nevertheless, *in vitro* and *in vivo* experiments show interactions between ZapA and ZapB (42, 58) and sequestration of ZapA by ZapB (55) that can reduce the stoichiometry up to 1:2. We take the intermediate value 1:1 for ZapA-FtsZ interaction.

We estimate the influence of ZapA proteins on the lateral bounds of FtsZ species from the *in vitro* experiments (31) that studied different stiffness of FtsZ/H6-ZapA structures by measuring their elastic modulus. At medium and long times, i.e., when bundling becomes important, FtsZ bundles without the presence of H6-ZapA had an average elastic modulus of ~ 9 dyn/cm². However, for a molar ratio of 1:1, the average elastic modulus was around 30 dyn/cm². Defining Δ_{ZapA} as the increment of the stiffness of FtsZ bundles by ZapA and taking as a reference the scenario without ZapA, we have a value of $\Delta_{\text{ZapA}} = 30/9 = 3.33$. Since ZapA molecules tend to connect pairs of FtsZ filaments instead of single filaments (53), we multiply this factor by the increment of lateral bond energy

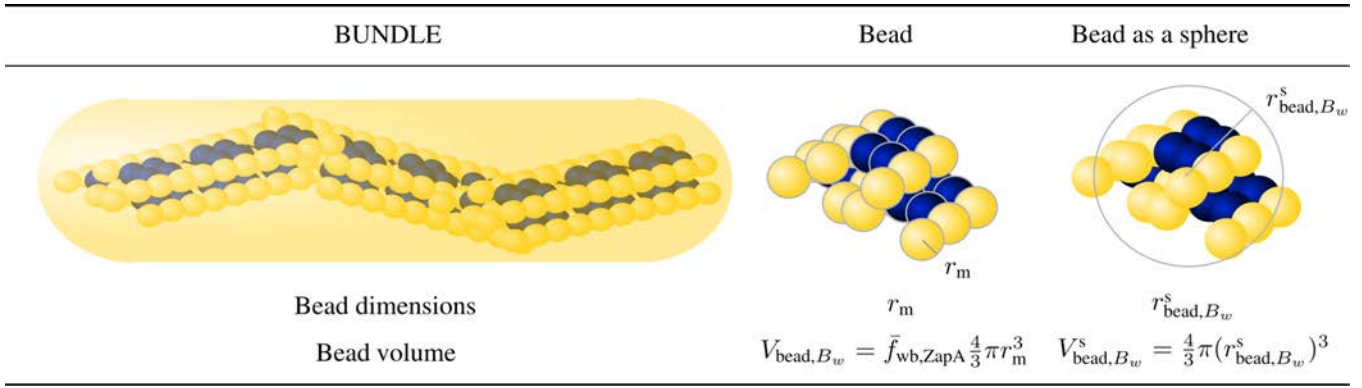


Fig. S8. Graphical representations of a bead in a three-dimensional structure made of cross-linked clusters of $\bar{f}_{\text{wb}, \text{ZapA}} = 36$.

associated to bundling of bundles of two or more filaments, i.e., $\Delta U_{b, \text{ZapA}} = \Delta_{\text{ZapA}} \Delta U_b$. Thus, we redefine the backward reaction rates as follows.

1. If a bundle of two filaments of average length \bar{L}_{fb}^m detaches laterally to form two independent filaments, i.e., if $P = B_2$, then

$$k_{\text{bu}}^- = k_{\text{bu}}^{0-} \begin{cases} 1 & \bar{L}_{\text{fb}}^m \leq 1, \\ e^{-(\bar{L}_{\text{fb}}^m - 1)U_b} & \bar{L}_{\text{fb}}^m > 1. \end{cases} \quad [\text{S72}]$$

If a bundle of three filaments of average length \bar{L}_{fb}^m detaches laterally to form a filament and a bundle, i.e., if $P = B_3$, then

$$k_{\text{bu}}^- = k_{\text{bu}}^{0-} e^{-\Delta U_{b, \text{ZapA}}} \begin{cases} 1 & \bar{L}_{\text{fb}}^m \leq 1, \\ e^{-(\bar{L}_{\text{fb}}^m - 1)(U_b + \Delta U_{b, \text{ZapA}})} & \bar{L}_{\text{fb}}^m > 1. \end{cases} \quad [\text{S73}]$$

2. Wide bundles are mainly present at long times and high concentrations. The tendency of ZapA proteins to make stiff bundles and to stabilize longitudinal bonds between FtsZ monomers (31) suggests that the average length of the species remains practically constant once ZapA proteins get attached to them. Our *in vitro* study demonstrated that bundles of pairs of filaments start forming at $C_{\text{tot}} = 2 \mu\text{M}$. At that concentration the average length of filaments and bundles is estimated by our model to be $\bar{L}_{\text{fb}}^m = 25$. Moreover, ZapA intervenes in bundling process when bundles are made of at least 2 filaments (53). Therefore, we set $\bar{L}_{\text{fb}}^m = 25$ as the expected length for wide bundles at steady state. Thus, if a wide bundle of average number of filaments $\bar{f}_{\text{wb}, \text{ZapA}}$ and average length \bar{L}_{fb}^m detaches laterally to form a filament and another bundle, i.e., if $P = B_w$, $R_1 = F$ and $R_2 = B_w$, then

$$k_{\text{bu}}^- = k_{\text{bu}}^{0-} e^{-24(U_b + \Delta U_{b, \text{ZapA}}) - \Delta U_{b, \text{ZapA}}}, \quad [\text{S74}]$$

Here, we do not distinguish between two stages of bundling. We assume that filaments detach at the same rate from sheets ($\bar{d} = 2$) and from long cross-linked clusters ($\bar{d} = 3$), i.e., cross-links do not highly affect the detachment of thin filaments.

3. If a wide bundle of average number of filaments $\bar{f}_{\text{wb}, \text{ZapA}}$ and average length $\bar{L}_{\text{fb}}^m = 25$ detaches laterally to form

two bundles, i.e., if $P = B_w$, $R_1 = B_w$ and $R_2 = B_w$, then

$$k_{\text{bu}}^- = k_{\text{bu}}^{0-} e^{-[24(U_b + 2\Delta U_{b, \text{ZapA}}) + 2\Delta U_{b, \text{ZapA}}]} \left(1 - \frac{C_{\text{tot}, \text{CM}}^a}{C_{\text{tot}, \text{CM}}^a, \text{max}}\right) \quad [\text{S75}]$$

where only the proportion of wide bundles in sheet form ($\bar{d} = 2$, Eq. S71) is allowed to disassociate. The proportion of long cross-linked clusters ($\bar{d} = 3$, Eq. S71) is not considered in Eq. S75 since cross-links are very strong to allow cluster dissociation (59, 60).

References

1. A. Ruiz-Martinez, T. M. Bartol, T. J. Sejnowski, and D. M. Tartakovsky. Efficient multiscale models of polymer assembly. *Biophys. J.*, 110(1):185–196, 2016.
2. D. Needleman. The material basis of life. *Trends in Cell Biology*, 25(12):713–716, 2015.
3. Y. Chen and H. P. Erickson. Rapid *in vitro* assembly dynamics and subunit turnover of FtsZ demonstrated by Fluorescence Resonance Energy Transfer. *J. Biol. Chem.*, 280(23):22549–22554, 2005b.
4. S. Arumugam, Z. Petrásek, and P. Schwille. MinCDE exploits the dynamic nature of FtsZ filaments for its spatial regulation. *Proc. Natl. Acad. Sci. U.S.A.*, 111(13):1192–1200, 2014.
5. G. Lan, A. Dajkovic, D. Wirtz, and S. X. Sun. Polymerization and bundling kinetics of FtsZ filaments. *Biophys. J.*, 95:4045–4056, 2008.
6. A. Dajkovic, G. Lan, S. X. Sun, D. Wirtz, and J. Lutkenhaus. MinC spatially controls bacterial cytokinesis by antagonizing the scaffolding function of FtsZ. *Curr. Biol.*, 18:235–244, 2008.
7. C. Frieden and D.W. Goddette. Polymerization of actin and actin-like systems: evaluation of the time course of polymerization in relation to the mechanism. *Biochemistry*, 22:5836–5843, 1983.
8. S. H. Northrup and H. P. Erickson. Kinetics of protein-protein association explained by Brownian dynamics computer simulation. *Proc. Natl. Acad. Sci. U.S.A.*, 89(8):3338–3342, 1992.
9. L. Romberg and T. J. Mitchison. Rate-limiting guanosine 5'-triphosphate hydrolysis during nucleotide turnover by FtsZ, a prokaryotic tubulin homologue involved in bacterial cell division. *Biochemistry*, 43:282–288, 2004.
10. P. Mateos-Gil, A. Paez, I. H. Zrger, G. Rivas, M. Vicente, P. Tarazona, and M. Vélez. Depolymerization dynamics of individual filaments of bacterial cytoskeletal protein FtsZ. *Proc. Natl. Acad. Sci. U.S.A.*, 109(21):8133–8138, 2012.
11. H. P. Erickson. Modeling the physics of FtsZ assembly and force generation. *Proc. Natl. Acad. Sci. U.S.A.*, 106(23):9238–9243, 2009.
12. E. Fischer-Friedrich, B. M. Friedrich, and N. S. Gov. FtsZ rings and helices: physical mechanisms for the dynamic alignment of biopolymers in rod-shaped bacteria. *Phys. Biol.*, 9(1), 2012.
13. Y. Chen, K. Bjornson, S. D. Redick, and H. P. Erickson. A rapid fluorescence assay for FtsZ assembly indicates cooperative assembly with a dimer nucleus. *Biophys. J.*, 88:505–514, 2005a.
14. S. Huecas, O. Llorca, J. Boskovic, J. Martin-Benito, J. M. Valpuesta, and J. M. Andreu. Energetics and geometry of FtsZ polymers: nucleated self-assembly of single protofilaments. *Biophys. J.*, 94:1796–1806, 2008.
15. D. Popp, M. Iwasa, A. Narita, H. P. Erickson, and Y. Maéda. FtsZ condensates: an *in vitro* electron microscopy study. *Biopolymers*, 91(5):340–350, 2009.
16. L. Romberg, M. Simon, and H. P. Erickson. Polymerization of FtsZ, a bacterial homolog of tubulin: Is assembly cooperative? *J. Biol. Chem.*, 18(15):11743–11753, 2001.
17. Y. Chen and H. P. Erickson. FtsZ filament dynamics at steady state: subunit exchange with and without nucleotide hydrolysis. *Biochemistry*, 48(28):6664–6673, 2009.
18. R. Mercier, M-A Petit, S. Schbath, S. Robin, M. El Karoui, F. Bocard, and O. Espéli. The MatP/matS site-specific system organizes the terminus region of the *E. coli* chromosome into a macrodomain. *Cell*, 135:475–485, 2008.

19. M. W. Bailey, P. Bisicchia, B. T. Warren, D. J. Sherratt, and J. Männik. Evidence for divisome localization mechanisms independent of the Min system and SlmA in *Escherichia coli*. *PLoS Genet.*, 10(8):e1004504, 2014.
20. J. Männik and M.W. Bailey. Spatial coordination between chromosomes and cell division proteins in *Escherichia coli*. *Front. Microbiol.*, 6(306), 2015.
21. O. Espeli, R. Borne, P. Dupaigne, A. Thiel, E. Gigant, R. Mercier, and F. Boccard. A MatP-divisome interaction coordinates chromosome segregation with cell division in *E. coli*. *EMBO J.*, 31:3198–3211, 2012.
22. R. Tsukanov, G. Reshes, G. Carmon, E. Fischer-Friedrich, N. S. Gov, I. Fishov, and M. Feingold. Timing of Z-ring localization in *Escherichia coli*. *Phys. Biol.*, 8:13, 2011.
23. L. Robert, M. Hoffmann, N. Krell, S. Aymerich, J. Robert, and M. Doumic. Division in *Escherichia coli* is triggered by a size-sensing rather than a timing mechanism. *BMC Biol.*, 12(17), 2014.
24. G. Fu, T. Huang, J. Buss, C. Coltharp, Z. Hensel, and J. Xiao. In vivo structure of the *E. coli* FtsZ-ring revealed by photoactivated localization microscopy (PALM). *PLoS ONE*, 5(9):e12680, 2010.
25. C. Coltharp, J. Buss, T. M. Plumer, and J. Xiao. Defining the rate-limiting processes of bacterial cytokinesis. *Proc. Natl. Acad. Sci. U.S.A.*, 113(8):1044–1053, 2016.
26. C. E. Dow, A. Rodger, D. I. Roper, and H. A. van den Berg. A model of membrane contraction predicting initiation and completion of bacterial cell division. *Integr. Biol.*, 5:2778–795, 2013.
27. S. Rueda, M. Vicente, and J. Mingorance. Concentration and assembly of the division ring proteins FtsZ, FtsA, and ZipA during the *Escherichia coli* cell cycle. *J. Bacteriol.*, 185(11):3344–3351, 2003.
28. C. A. Hale and A. J. de Boer. Direct binding of Ftsz to ZipA, an essential component of the septal ring structure that mediates cell division in *E. coli*. *Cell*, 88(2):175–185, 1997.
29. C. T. Culbertson, S. C. Jacobson, and J. M. Ramsey. Diffusion coefficient measurements in microfluidic devices. *Talanta*, 56:365–373, 2002.
30. L. Niu and J. Yu. Investigating intracellular dynamics of FtsZ cytoskeleton with photoactivation single-molecule tracking. *Biophys. J.*, 95(4):2009–2016, 2008.
31. A. Dajkovic, S. Pichoff, J. Lutkenhaus, and D. Wirtz. Cross-linking FtsZ polymers into coherent Z rings. *Molec. Microbiol.*, 78(3):651–668, 2010.
32. I. V. Surovtsev, J. J. Morgan, and P. A. Lindhal. Kinetic modeling of the assembly, dynamic steady state and contraction of the FtsZ ring in prokaryotic cytokinesis. *PLoS Comput. Biol.*, 4(7), 2008.
33. C.S.G. Addinall, C. Cao, and J. Lutkenhaus. Temperature shift experiments with an ftsZ84(Ts) strain reveal rapid dynamics of FtsZ localization and indicate that the Z ring is required throughout septation and cannot reoccupy division sites once constriction has initiated. *J. Bacteriol.*, 179(13):4277–4284, 1997.
34. Q. Sun and W. Margolin. FtsZ dynamics during the division cycle of live *Escherichia coli* cells. *J. Bacteriol.*, 180(8):2050–2056, 1998.
35. M. Loose and T.J. Mitchinson. The bacterial cell division proteins FtsA and FtsZ self-organize into dynamic cytoskeletal patterns. *Nature Cell Biol.*, 16(1):38–46, 2014.
36. H. P. Erickson, D. E. Anderson, and M. Osawa. FtsZ in bacterial cytokinesis: cytoskeleton and force generator all in one. *Microbiol. Mol. Biol. Rev.*, 74(4):504–528, 2010.
37. J. Stricker, P. Maddox, E. D. Salmon, and H. P. Erickson. Rapid assembly dynamics of the *Escherichia coli* FtsZ-ring demonstrated by fluorescence recovery after photobleaching. *Proc. Natl. Acad. Sci. U.S.A.*, 99(5):3171–3175, 2002.
38. D. E. Anderson, F. J. Gueiros-Filho, and H. P. Erickson. Assembly dynamics of FtsZ rings in *Bacillus subtilis* and *Escherichia coli* and effects of FtsZ-regulating proteins. *J. Bacteriology*, 186(17):5775–5781, 2004.
39. J. M. González, M. Vélez, M. Jiménez, C. Alfonso, P. Schick, J. Mingorance, M. Vicente, A. P. Minton, and G. Rivas. Cooperative behavior of *Escherichia coli* cell-division protein ftsz assembly involves the preferential cyclization of long single-stranded fibrils. *Proc. Natl. Acad. Sci. U.S.A.*, 102(6):1895–1900, 2005.
40. C. Lu, M. Reedy, and H. P. Erickson. Straight and curved conformations of FtsZ are regulated by GTP hydrolysis. *J. Bacteriol.*, 182(1):164–170, 2000.
41. K-H. Huang, J. Durand-Heredia, and A. Janakiraman. FtsZ ring stability: of bundles, tubules, crosslinks and curves. *Journal of Bacteriology*, 195(9):1859–1868, 2013.
42. J. Buss, C. Coltharp, T. Huang, C. Pohlmeier, S-C. Wang, C. Hatem, and J. Xiao. In vivo organization of the FtsZ-ring by ZapA and ZapB revealed by quantitative super-resolution microscopy. *Molecular Microbiol.*, 89(6):1099–1120, 2013.
43. H. P. Erickson, D. W. Taylor, K. A. Taylor, and D. Bramhill. Bacterial cell division protein FtsZ assembles into protofilament sheets and minirings, structural homologs of tubulin polymers. *Proc. Natl. Acad. Sci. U.S.A.*, 93:519–523, 1996.
44. Z. Li, M. J. Trimble, Y. V. Brun, and G. J. Jensen. The structure of FtsZ filaments in vivo suggests a force-generating role in cell division. *EMBO J.*, 26:4694–4708, 2007.
45. J. M. González, M. Jiménez, M. Vélez, J. Mingorance, J. M. Andreu, M. Vicente, and G. Rivas. Essential cell division protein FtsZ assembles into one monomer-thick ribbons under conditions resembling the crowded intracellular environment. *J. Biol. Chem.*, 278(39):37664–37671, 2003.
46. R. J. Ellis. Macromolecular crowding: an important but neglected aspect of the intracellular environment. *Curr. Opin. Struct. Biol.*, 11:114–119, 2001.
47. I. Terakoa. *Polymer Solutions: An Introduction to Physical Properties*. John Wiley & Sons, Inc., 2002.
48. K. Kremer and G. S. Grest. Dynamics of entangled linear polymer melts: A molecular-dynamics simulation. *The Journal of Chemical Physics*, 92(8):5057–5086, 1990.
49. F. Perrin. Mouvement brownien d'un ellipsoïde (ii). rotation libre et dépolariation des fluorescences. translation et diffusion de molécules ellipsoïdales. *Journal de Physique et Le Radium*, 7(1):1–11, 1936.
50. S. Hansen. Translational friction coefficients for cylinders of arbitrary axial ratios estimated by Monte Carlo simulation. *J. Chem. Phys.*, 121(18):9111–9115, 2004.
51. M. A. van Dijk and A. Wakker. *Concepts in Polymer Thermodynamics*, volume 2. Technomic Publishing Company, Inc., 1997.
52. S. M. Bhattacharjee, A. Giacometti, and A. Maritan. Flory theory for polymers. *J. Phys. Condens. Matter*, 25(50), 2013.
53. T. Mohammadi, G. E. J. Ploeger, J. Verheul, A. D. Comvalius, A. Martos, C. Alfonso, J. van Marle, G. Rivas, and T. den Blaauwen. The GTPase activity of *Escherichia coli* FtsZ determines the magnitude of the FtsZ polymer bundling by ZapA in vitro. *Biochemistry*, 48:11056–11066, 2009.
54. H. H. Low, M. C. Moncrieffe, and J. Lowe. The crystal structure of ZapA and its modulation of FtsZ polymerisation. *J. Molec. Biol.*, 341:839–852, 2004.
55. E. Galli and K. Gerdes. FtsZ-ZapA-ZapB interactome of *Escherichia coli*. *J. Bacteriol.*, 194(2):292–302, 2012.
56. F. J. Gueiros-Filho and R. Losick. A widely conserved bacterial cell division protein that promotes assembly of the tubulin-like protein FtsZ. *Genes Dev.*, 16(19):2544–2556, 2002.
57. R. Pacheco-Gómez, X. Cheng, M. R. Hicks, C. J. I. Smith, D. I. Roper, S. Addinall, A. Rodger, and T. R. Dafforn. Tetramerization of ZapA is required for FtsZ bundling. *Biochem. J.*, 449(13):795–802, 2013.
58. J. Buss, C. Coltharp, G. Shtengel, X. Yang, H. Hess, and J. Xiao. A multi-layered protein network stabilizes the *Escherichia coli* FtsZ-ring and modulates constriction dynamics. *PLoS Gen.*, 11(4):795–802, 2015.
59. T. T. Falzone, M. Lenz, D. R. Kovar, and M. L. Gardel. Assembly kinetics determine the architecture of α -actin in crosslinked F-actin networks. *Nature Comm.*, 3(861):266–272, 2012.
60. M. H. Jensen, E. J. Morris, and D. A. Weitz. Mechanics and dynamics of reconstituted cytoskeletal systems. *Biochim. Biophys. Acta*, 1853(11):3038–3042, 2015.